INTERPRETING THERMODENUDER DATA WITH AN OPTIMIZING INSTRUMENT MODEL

A Thesis
Presented to
The Academic Faculty

By

James Ricky Hite, Jr.

In Partial Fulfillment
Of the Requirements for the Degree
Master of Science in Earth and Atmospheric Sciences

Georgia Institute of Technology

December 2012

INTERPRETING THERMODENUDER DATA WITH AN OPTIMIZING INSTRUMENT MODEL

Approved by:

Dr. Athanasios Nenes
School of Earth and Atmospheric Sciences
Georgia Institute of Technology

Dr. Nga Lee Ng
School of Earth and Atmospheric Sciences
Georgia Institute of Technology

Dr. Michael Bergin
School of Earth and Atmospheric Sciences
Georgia Institute of Technology

Date Approved: November 12, 2012

ACKNOWLEDGEMENTS

I would like to acknowledge the financial support of EAS department in allowing me to serve at a teaching assistant throughout my time as a Master's student. The continuing encouragement and counseling from my advisor, Dr. Nenes, has been greatly appreciated and was pivotal in the completion of this work. Of course, I would be remiss to exclude the mentoring of several other members of the group, including Terry Lathem, Shannon Capps, and Kate Cerully – without whom the presented work would not have been the same.

TABLE OF CONTENTS

LIST OF TABLES

LIST OF FIGURES

LIST OF SYMBOLS AND ABBREVIATIONS

AIM	Aerosol Instrument Manager
C	Cost function minimized by the optimization routine
$\bar{c}_A$	Thermal speed of the volatilizing compound in air
CCN	Cloud condensation nuclei
CFD	Computational fluid dynamics
c_p	Specific heat capacity of air
CPC	Condensation particle counter
CTM	Chemical Transport Model
D_{AB}, D	Diffusion coefficient, volatilizing component in air
DMA	Differential mobility analyzer
D_p	Diameter of aerosol particle
$D_{p,in}$	Aerosol diameter entering the TD, measured
D_{pm}	Modeled outlet diameter
$D_{p,out}$	Aerosol diameter exiting the TD, measured
$D_{p,resid}$	Residual aerosol diameter of the non-volatile core
$D_{p,2x}$	Model-predicted outlet diameter for the double-charged aerosol
HBS	Hirschfelder, Bird, and Spotz
ΔH_v	Specific enthalpy of vaporization
J	Jacobian matrix returned by optimization routine
k	Thermal conductivity of air adjusted for non-continuum effects
k_a	Thermal conductivity of air in the continuum regime

Kn	Knudsen number
LPM	Liters per minute
M	Number of independent observations used in the model optimization
M	Molar mass / molecular weight of aerosol component
M_a	Molar mass / molecular weight of air
m_{evap}	Mass concentration change of the volatilizing aerosol
N	Number of parameters fit in the model optimization
OA	Organic Aerosol
P	Pressure
P_∞^o, P_{sat}	Saturation vapor pressure of volatilizing species far from the aerosol
$P_{B,\infty}$	Vapor pressure of volatilizing species far from the aerosol
$\vec{P}^N$	Fitted parameters in the subroutine optimization space
Q_{set}	Volumetric flow rate setpoint
R	Ideal gas constant
R_n	Equilibrium ratio of the volatilizing aerosol component
R_{TD}	Inner radius of thermodenuder heating section
r	Radial distance from the centerline
SI	International System (of units)
SIMPLE	Semi-Implicit Method for Pressure Linked Equations
SMPS	Scanning mobility particle sizer
SOA	Secondary Organic Aerosol
T	Temperature
T_{set}	Setpoint temperature of the thermodenuder

T_∞	Temperature far from aerosol
TD	Thermodenuder
U, u, u_z	Axial velocity
V, v	Radial velocity
v_A	Diffusion volume of air
v_B	Diffusion volume of aerosol component
VBS	Volatility Basis Set
VOC	Volatile Organic Carbon
VTDMA	Volatility Tandem Differential Mobility Analyzer
x, x_j, $\vec{x}^N$	Optimized volatility parameter(s)
Y, (Y_i)	Residuals vector (component) used in the optimization routine
α	Accommodation / evaporation coefficient
α_T	Thermal accommodation coefficient
λ_{AB}	Mean free path of volatilizing component in air
μ	Kinematic viscosity of air
ρ	Density
ρ_{resid}	Density of the non-volatile residual matter
σ	Interfacial energy
Φ	Fuchs-Sutugin correction factor for non-continuum mass transfer

SUMMARY

Secondary organic aerosol (SOA) generated through the partitioning of gas phase volatile organic carbon compounds (VOCs) into the condensed phase has both epidemiological and climatic impacts through the growth of particulate matter into relevant sizes for respiratory interactions and cloud condensation nuclei activity. Considering the complex chemistry involved with VOC oxidation and subsequent formation of SOA, bulk properties like oxidation state, often represented by O:C ratio, and volatility are used to simplify the representation of SOA in chemical transport models (CTMs) and the like [e.g. Tsimpidi et al. 2010]. This preference for bulk properties is supported by the availability of ambient measurement techniques to constrain model parameters and scenarios. The volatility of SOA is often described by treating it as a mixture of components with differing partitioning coefficients through the volatility basis set (VBS) approach rather than explicitly resolving the complex chemistry [Donahue et al., 2006]. This study presents a method of determining the volatility of an aerosol sample through the use of an optimizing thermodenuder (TD) instrument model that is used to fit laboratory data. Data collected using a volatility tandem differential mobility analyzer (VTDMA) setup consist of inlet and outlet particle size and number concentrations for select dicarboxylic acids – compounds known to contribute to atmospheric SOA. These are interpreted by the model through an iterative optimization routine to obtain estimates of volatility parameters (e.g. saturation concentrations) which are compared to available literature data. The instrument model is currently divided into two decoupled modules. The first resolves the flow field characteristics, obtaining the temperature profile,

pressure variations, and radial velocity distribution of the TD, and the second resolves the gas to particle partitioning of aerosol with a given condensed-phase volatility distribution in the TD using the VBS approach as described in the literature. Solving the full hydrodynamic equations for the flow characteristics provides a better numeric representation of entry length and radial velocity variations and is an improvement over similar TD modeling studies in the literature. However, results indicate that coupling the two modules is necessary to more accurately resolve the suppression of evaporation due to buildup of organic vapors in the TD, even at the low mass concentrations involved with the presented experiments.

INTRODUCTION

Atmospheric aerosols affect climate through their direct interactions with solar radiation and by modulating cloud microphysics, ultimately changing cloud properties like albedo, precipitation frequency, vertical extent, and lifetime. These effects act as feedback mechanisms between different components of the climate system in complex ways, presenting a problem for climate modeling in general and introducing uncertainty in determining the direction and magnitude of climate change, natural or anthropogenic [Jimenez et al., 2009; IPCC, 2007; Kanakidou et al., 2005]. Organic aerosol (OA) in particular presents the greatest challenge in terms of chemical complexity and its effect, for instance, on cloud condensation nuclei (CCN) activity [e.g., Riipinen et al., 2011]. The formation of secondary organic aerosol (SOA) as part of photochemical smog in urban areas also impacts human health [e.g., Hallquist et al., 2009]. SOA forms from the nucleation of volatile organic compounds (VOCs), typically onto preexisting aerosol. This transition from the gas to particle phase is dependent upon the volatility of the organic compound, described by partitioning theory for complex, multicomponent OA [Donahue et al., 2006: Pankow, 1994].

SOA volatility is often investigated with the use of a thermodenuder (TD) [e.g. Salo et al., 2011; Cappa and Jimenez, 2010]. A thermodenuder is essentially a laminar flow reactor that is maintained at a well-controlled temperature setpoint (T_{set}) in order to quantify aerosol volatilization [Huffman et al., 2008; Faulhaber et al., 2009; An et al., 2007]. These measurements do not necessarily require a priori knowledge of the exact

chemical composition of the aerosol in order to describe its volatility in accordance with the volatility basis set approach (VBS) [Donahue et al., 2006]. The heating section of a TD is often followed by a cooling section, sometimes containing activated carbon to absorb and remove the volatilized vapors from the sample flow, leaving the organic aerosol behind with the goal of prohibiting re-condensation of the vapors onto the aerosol during the temperature drop after leaving the heating section. The necessity and design of this cooling section is heavily debated in the literature mostly out of concerns regarding the potential occurrence of re-evaporation or re-condensation [e.g., Fuentes and McFiggans, 2012; Saleh et al., 2011; Fierz et al., 2007]. Ideally, neither should occur. In this study, the TD involved in the aerosol measurements makes use of a cooling section. However, the instrument model only resolves the heating section. The cooling section is assumed to merely maintain the output from the heating section, not modify it further.

Different TD models have been implemented in the literature making a range of assumptions and approximations about the flow conditions in the instrument. Cappa et al. [2010] simulates the TD temperature distribution with a piecewise approximated temperature profile with constant radial temperature based on the experimental temperature profile of Huffman et al. [2008]. Riipinen et al. [2010] assumes a constant temperature throughout the TD. Fuentes and McFiggans [2012] choose a plug flow in their model, noting the deviation from reality and how it impacts the volatility of their model aerosol, in order to simplify the calculations.

Limitations on aerosol volatilization within the TD have been investigated with various conclusions [e.g., Saleh et al., 2011; Cappa et al., 2010; Riipenen et al., 2010; Saleh and Shihadeh, 2007]. In general, aerosol volatilization in the TD may be limited

either through equilibration with the surrounding vapor phase or by evaporation kinetics. The likelihood of a thermodynamic or kinetic limitation on aerosol volatilization is linked to the volatility of the particular aerosol, mass concentration of the sample, geometry of the TD, volumetric flow rate, and temperature set point of the instrument. To determine the limitations on aerosol volatilization other studies typically sacrifice the physical consistency of the instrument flow conditions to better handle the gas-particle partitioning, or adjusting the laboratory procedure to isolate particular variables and simplify the necessary assumptions [Saleh et al. 2008].

The goal of this work is to develop a fully coupled instrument model that resolves the pressure, temperature, and velocity fields within the TD along with the mass transfer between the volatilizing aerosol and vapor phase component. Presented herein are the first steps towards achieving this goal.

CHAPTER 2: METHODOLOGY

2.1 Thermodenuder Instrument Model

The thermodenuder (TD) model consists of two modules: one that determines the flow characteristics inside the heating section for a given temperature and volumetric flow rate setpoint and a second that models the evaporation of aerosol through the heating section. The modules are run separately, providing the advantage of resolving the flow field once for a given setpoint while being able to vary the input into the evaporation module.

2.1.1 Flow Field Module

The flow and temperature fields in the instrument are determined by numerically solving the Navier-Stokes equations for an equilibrium state at a given set point (see Appendix A for equations). The boundary conditions to the flow problem are the room-temperature centerline velocity, which is calculated from the flow rate and heating section geometry, and the scaled wall temperature profile obtained from earlier measurements. The solution is obtained using the Semi-Implicit Method for Pressure Linked Equations (SIMPLE) [Patankar, 1980] for an axisymmetric flow with a particular choice of equation solvers and under relaxation parameters; however, the time required for convergence to a solution is on the order of several minutes. Figure 1 shows the reduction of the sum of squares residuals of the flow domain against the number of iterations, and Figure 2 shows the convergence of those parameters to a particular value with increasing number of iterations. The variables at the reference point are: U – the axial velocity along the flow, V – the radial velocity, M/P – the gauge pressure at that point (associated with mass conservation), and T – the absolute temperature; all units are SI.

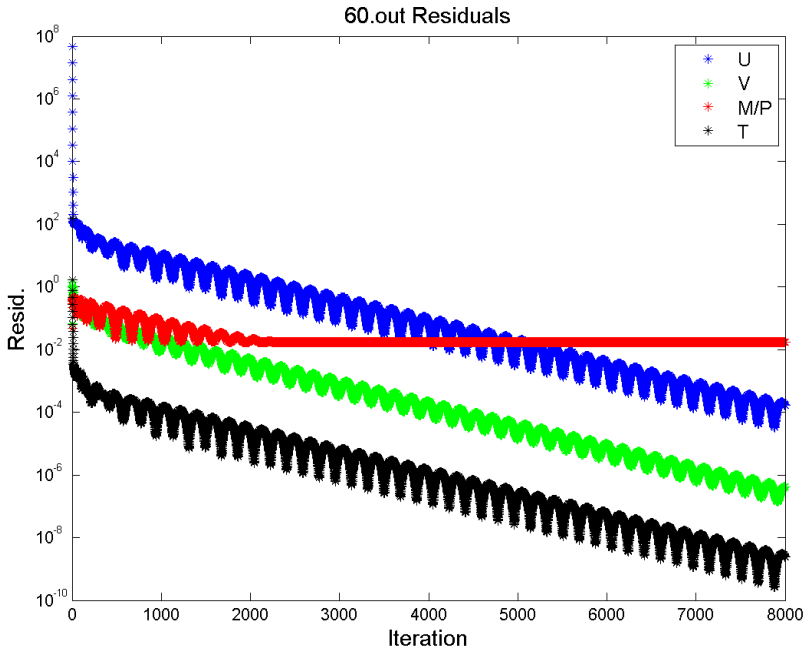

Figure 1: Convergence of full flow solution illustrated by reduction of residuals

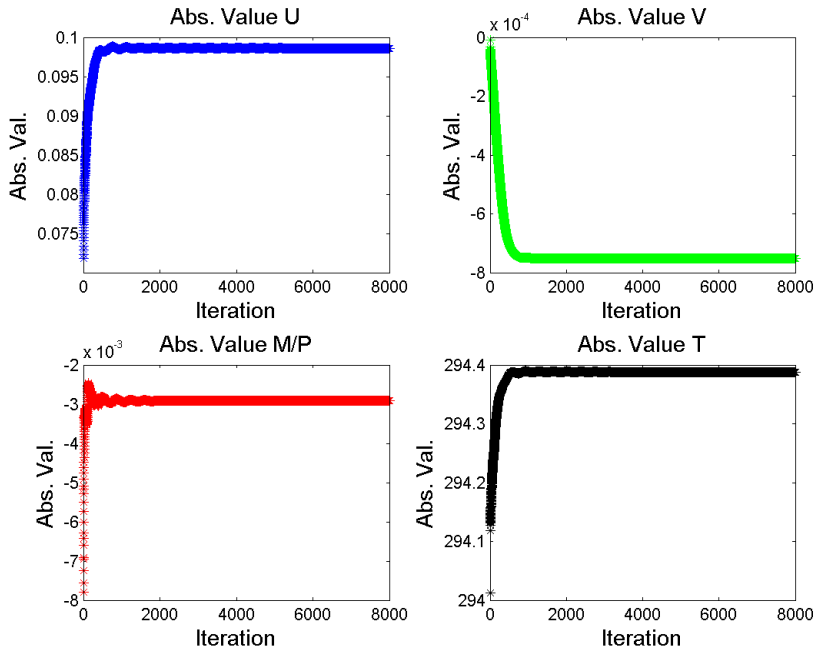

Figure 2: Convergence of full flow solution at a reference point

In the current decoupled model state, the convergence time does not necessarily need to be short as the flow characteristics (*P, T, U*) are stored after being calculated and then simply referenced by the evaporation module. If the modules are to be combined however, accounting for the mass transfer of the aerosol from the condensed to the vapor phase or vice versa would require either updating the flow field simultaneously or iteratively with the evaporation module. Such an approach, though, would need to minimize the convergence time in order to be feasible when considering the additional cost of the model optimization. Thus, the need for a quick solution is a practical concern for model deployment; therefore, a simplified problem is then considered to make the calculation converge more quickly. Beginning with an idealized, fully developed laminar flow with centerline velocity equal to that determined by the flowrate and instrument geometry, only the temperature diffusion from the wall is considered in the solution of the energy balance. This partial solution converges in seconds, requiring two orders of magnitude fewer iterations than the full solution. Figures 3 and 4 show the same data for the partial solution as Figures 1 and 2 showed for the full solution (the two figures show results for different temperature setpoints, but these results did not vary qualitatively with temperature setting). The partial solution convergence is bolstered by not including other variables in the calculation, and therefore their absolute values do not change with the number of iterations. To determine whether the partial solution is an applicable substitute for the full calculation, differences in the two are investigated by comparing the temperature distribution at three set points used in accompanying laboratory measurements. Deviations from laminar flow resultant from calculating the full solution are also depicted by comparing *U*, *V*, and *P*.

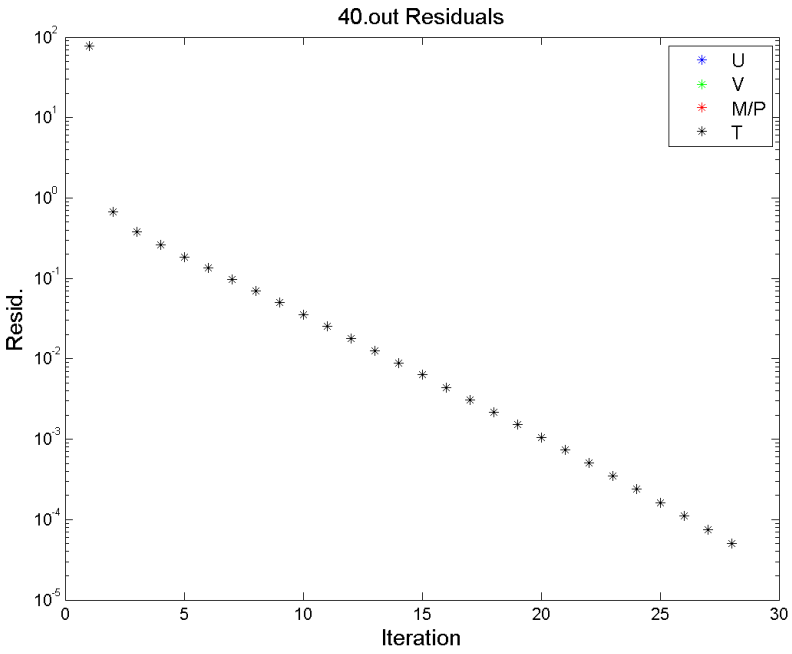

Figure 3: Convergence of partial flow solution illustrated by reduction of residuals

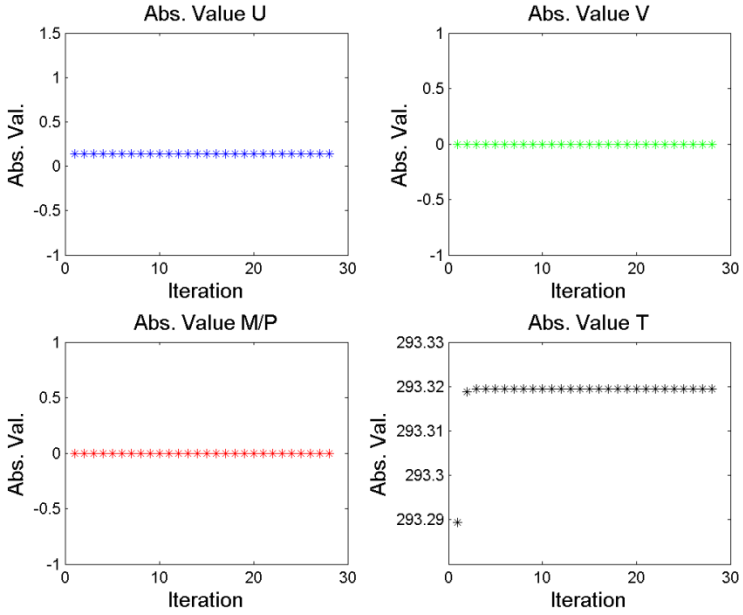

Figure 4: Convergence of partial flow solution at a reference point

An example of the temperature distribution in the TD generated by the model is given in Figure 5. The notation used in the figure title is held over from another analysis where different grid resolutions were compared in the flow field module; it indicates 100 radial and axial grid points were used to resolve the flow for the full solution ("both" represents the full calculation). Temperature distributions generated from the full or partial solutions were visually indistinguishable, so comparisons were made by taking the residual between the two solutions at different temperature setpoints.

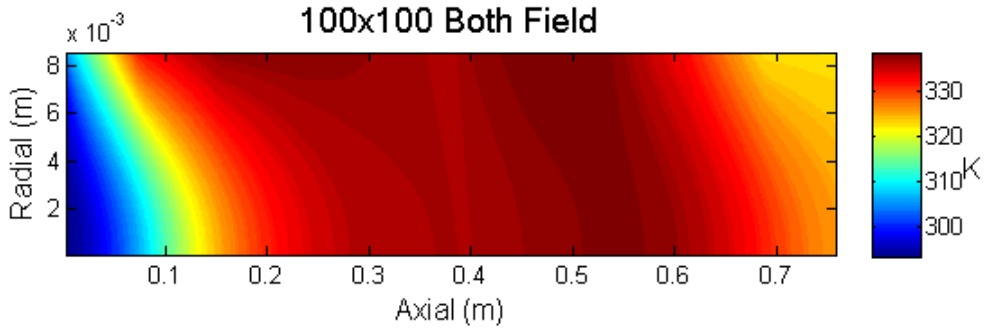

Figure 5: Example axisymmetric temperature distribution in TD for 60°C setpoint

Differences in the temperature distribution from the full or partial flow field calculations are compared against those associated with changes in the inlet temperature in order to place them in the context of experimental conditions where variations in room temperature on the order of 5°C were observed over the course of measurements. Residuals in the flow fields calculated for inlet temperatures of 293 and 298K (the base value) are compared alongside the residuals of the full and partial solutions for the temperature settings of 40, 50, and 60°C in Figures 6, 7 and 8 respectively.

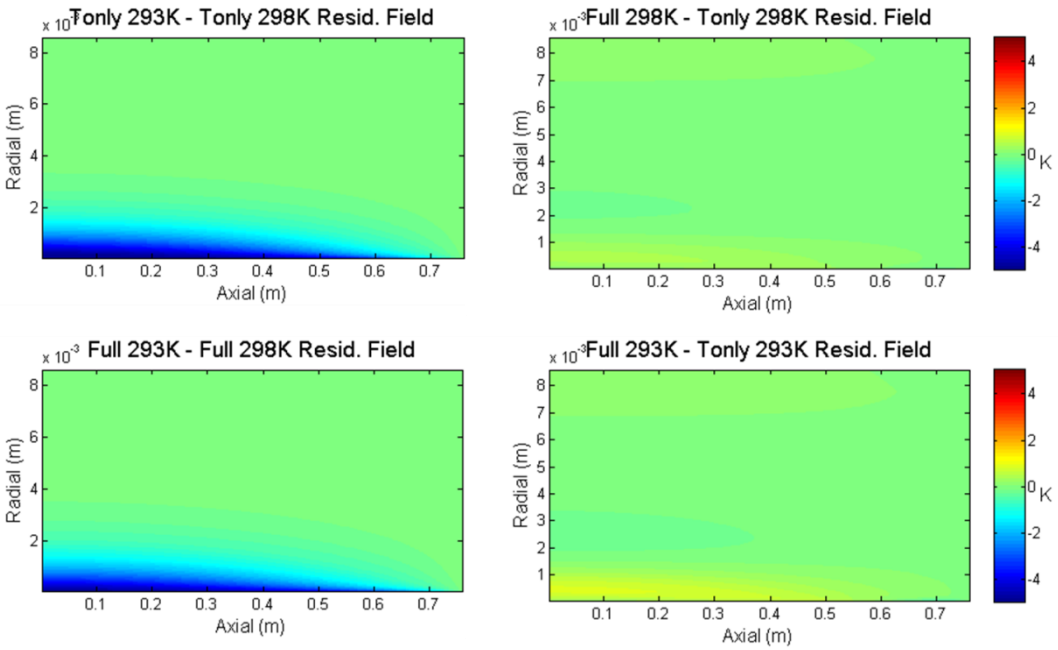

Figure 6: TD model flow field residuals for 40°C setpoint

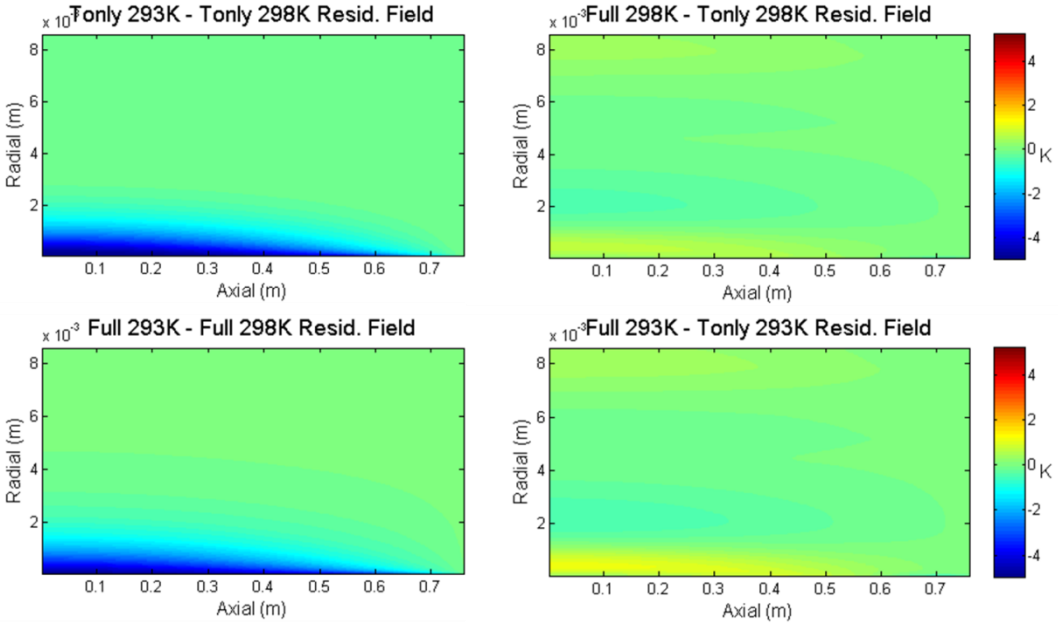

Figure 7: TD model flow field residuals for 50°C setpoint

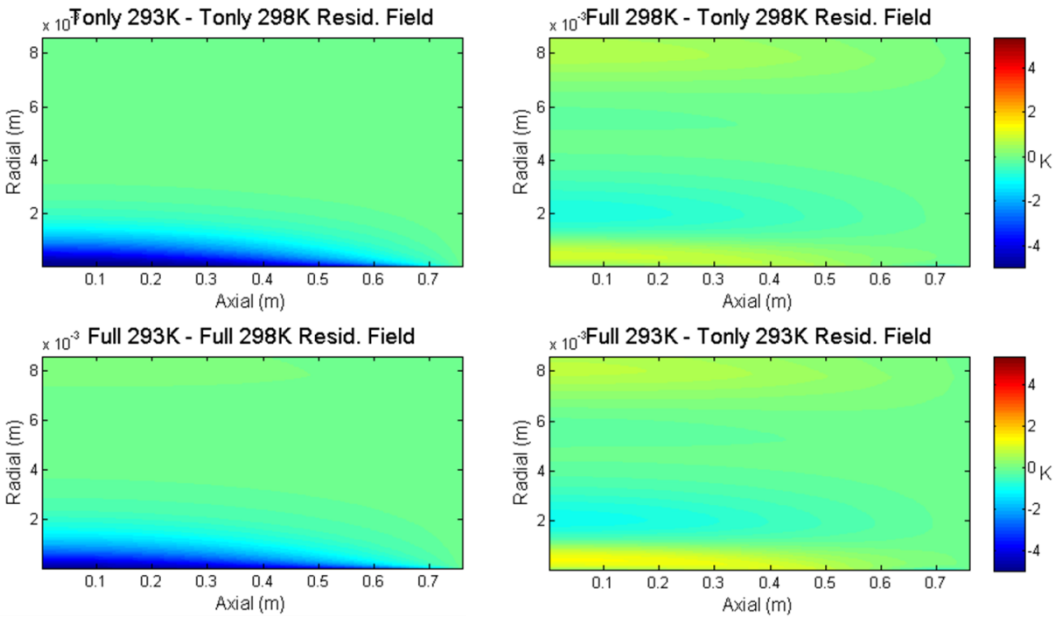

Figure 8: TD model flow field residuals for 60°C setpoint

The effect of decreasing the inlet temperature appears to cause a decrease in the centerline temperature throughout the TD on the order of the temperature change (~4 K). This is consistent with the simple physical expectation of a cooler inlet temperature. Whereas, the full/partial solution residuals appear to have a particular pattern that consists of warmer temperatures near the centerline and wall with cooler temperatures in between. However, the magnitude of these variations is smaller than those associated with a simple variation of inlet temperature (~± 2 K). There also appears to be an increase in the magnitude of the variations with an increase in the setpoint temperature (T_{set}) as can be seen from visual inspection of the above figures. An explanation of these variations lies in the deviation of the flow from ideal laminar conditions (which is the assumption of the partial calculation). In the full calculation, the axial velocity (U) increases along the length of the TD, an acceleration that is consistent with both the

calculated pressure gradient and negative radial velocity (*V*, towards the centerline). This acceleration is consistent with flow expansion as it passes through the TD – an explanation that has been interpreted as a temperature-dependent flow rate in the literature [e.g. Cappa 2010]. A confirmation of this thermal acceleration can be derived from Figures 9 and 10 which shows the percent difference between the calculated (full) and ideal laminar (partial) axial velocity fields.

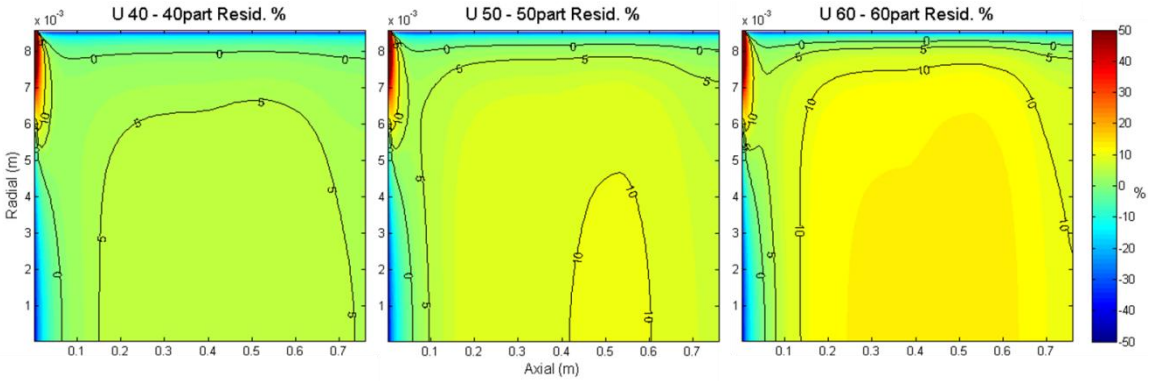

Figure 9: Percent difference between calculated and laminar axial flow velocity at inlet temperature of 298K

Aside from the boundary effects, the axial velocity appears to increase in the full solution compared to the partial calculation. With increasing T_{set}, the axial velocity increases to a greater extent over the ideal laminar value, and it increases even further when the inlet temperature is decreased. A greater increase in the axial velocity is expected to be associated with a lower initial temperature and greater final temperature (setpoint) when considering thermal expansion. The greater increase in *U* presented in Figure 10 when compared to Figure 9 illustrates this. This acceleration of the flow also explains the

decrease in the temperature between the centerline and the wall of the TD as seen in Figures 6 through 8 through an increase in the entry length.

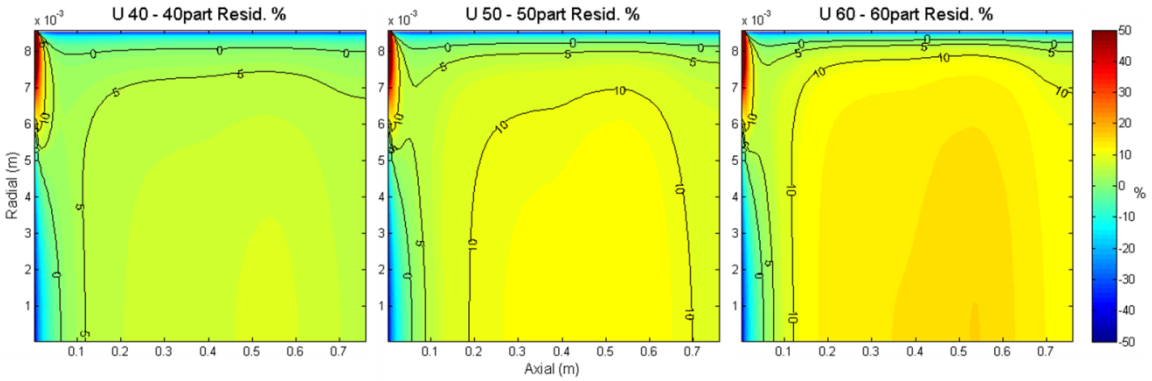

Figure 10: Percent difference between calculated and laminar axial flow velocity at inlet temperature of 293K

The boundaries of the residual plots are similar at all conditions in Figures 9 and 10; thus, they do not appear to be temperature dependent. A physical explanation for the occurrence of the zero velocity region near the TD wall (highest radial distance, top of Figures 9 and 10) is probably the development of a boundary layer in the calculation. It appears to be consistent with the warmer temperature residual in the comparisons of Figures 6 through 8 as the transfer of heat from the wall would be reduced with the development of a boundary layer. The variation in velocity near the inlet may not be realistic but may be a numeric phenomenon. In summary, the differences between the full and partial solution temperature distribution in the TD model flow field do not appear to be of greater magnitude than those predicted for differences in the inlet temperature. However, the deviations from ideal flow conditions may affect the volatilization of aerosol. This possibility will be further explored in the results. Once the flow is resolved, the evaporation module can then take into account variation in the temperature gradient

associated with entry length and the placement of the three thermistors as the aerosol moves through it.

2.1.2 Evaporation Module

While this is referred to as the "evaporation" module as a matter of convenience, the process that occurs is, more generally, volatilization as the numerical treatment could represent either liquid or solid aerosol partitioning to either a condensed or vapor phase. The aerosol volatilization is considered separately along each streamline of the flow in the TD. The observed aerosol distribution is discretized onto a number of aerosol size bins, each with a characteristic diameter and number concentration. The chemical composition, defined by properties such as molecular weight and density, for each aerosol section may be defined independently, but one set of values is used for all sections when considering a single component aerosol population in this study. The treatment for chemically complex aerosol will be addressed in an upcoming publication [Hite et al., In Prep.]. Evaporation of aerosol particles with a given initial diameter is modeled with the following differential equation:

$$D_p \frac{dD_p}{dt} = \frac{\frac{P_{B,\infty}}{P_\infty^o} - \exp\left(\frac{4M\sigma}{R\rho D_p T_\infty}\right)}{\frac{\rho R T_\infty}{4\mathcal{D}_{AB} M P_\infty^o \Phi} + \frac{\Delta H_v \rho}{4kT_\infty}\left(\frac{\Delta H_v M}{RT_\infty} - 1\right)} \quad (1)$$

where T_∞ is the air temperature inside the TD, P_∞^o is the saturation vapor pressure of the volatilizing species at T_∞, $P_{B,\infty}$ is the vapor pressure of the volatilizing species far from the surface of the particle, ΔH_v is the specific enthalpy of vaporization (J kg^{-1}), and R is the ideal gas constant. Variables with the subscript x_∞ represent properties of the background gas phase, far from the aerosol. ρ, D_p, M, and σ are the density, diameter, molar mass, and interfacial free energy of the aerosol component, respectively. The thermal conductivity of air is represented by k. D_{AB} is the diffusivity of the volatilizing

species in air. Φ is the value of the Fuchs-Sutugin correction factor. These three parameters are presented in more detail below.

The saturation vapor pressure is assumed to vary with temperature according to the integrated Clausius-Clapeyron relationship, making use of a reference saturation vapor pressure at 298K such that:

$$P_{\infty}^{o}(T_{\infty}) = P_{\infty}^{o}(298K)\left[\frac{M\Delta H_v}{R}\left(\frac{1}{298K} - \frac{1}{T_{\infty}}\right)\right] \quad (2)$$

The associated ΔH_v is assumed to be constant throughout the temperature range considered in order to treat it as a fitting parameter for the model optimization. This assumption can be relaxed for aerosol of known composition by incorporating its specific heat capacity. However, aerosol are exposed to a small temperature range in this study (~20K), and the method will be generalized to deal with ambient aerosol of potentially unknown chemical composition. Therefore, the temperature dependence of ΔH_v is not considered at this time.

The thermal conductivity, k, of air is given by

$$k = \frac{k_a}{1+\frac{2k_a}{\alpha_T D_p \rho c_p}\left(\frac{2\pi M_a}{RT_{\infty}}\right)^{1/2}} \quad (3)$$

where k_a is the thermal conductivity of air in the continuum regime, $k_a = 10^{-3}(4.39 + 0.071T)$ with units of J m^{-1} s^{-1} K^{-1}, c_p is the specific heat capacity of air with units of J kg^{-1} K^{-1}, and α_T is the thermal accommodation coefficient, here considered to be unity [Seinfeld and Pandis, 2006]. M_a is the molecular weight of air.

The diffusivity of the volatilizing compound in air as a function of temperature follows the method of Fuller et al. [1966] where the diffusion coefficients for a binary mixture of air (A) and the evaporating component (B) are given as:

$$D_{AB} = \frac{1\times10^{-3}T^{1.75}\left(\frac{1}{M_A}+\frac{1}{M_B}\right)^{1/2}}{P\left(v_A^{1/3}+v_B^{1/3}\right)^2} \quad (4)$$

where T is the temperature and P is the pressure at a particular point in the discretized flow, and v_B is the diffusion volume of a particular component. The diffusion volumes are empirically defined by Fuller et al. [1966] as the sum of contributions from individual atoms in a particular molecule along with modifications for certain structural features (e.g., rings); the equation returns values with units of $cm^2\ s^{-1}$. This method was presented as a more accurate estimation for binary diffusion than that of contemporaries at the time of publication. A study considering diffusivities of low volatility compounds in various background gases [Ravindran 1979], found that it was a comparably accurate estimation technique for diffusion in low molecular weight carrier gases. However, it was not the most accurate method, as the referenced study concluded that an empirical fit by Chen and Othmer [1962] more consistently fit their data. While both methods – Chen & Othmer and Fuller – are qualitatively similar to the often-cited Hirschfelder, Bird, and Spotz (HBS) formulation [Bird 2002], they make use of empirical fits to critical properties and diffusion volumes rather than the Lennard-Jones parameters. Whereas critical temperature values are not necessarily available for all desired chemical species, empirical diffusion volumes may be determined for nearly any arbitrary organic compound of interest, thus the latter is a more practical method for future generalization of the evaporation module to organic aerosol. The calculated diffusion volumes for each compound in this study are provided in Table 1 along with the densities and molecular weights. The calculation of the diffusion volumes are discussed in the referenced literature and an example is provided as supplementary material in Appendix B.

Table 1: Thermodynamic and transport properties of investigated compounds

Organic Acid	Molar Mass (kg mol^{-1})	Density (kg m^{-3})	Diffusion Volume (cm^{-3})*	Interfacial Energy (J m^{-2})**	Accommodation/ Evaporation Coefficient***
Adipic	0.14614	1362	140.72	0.06 (0.06)[A] 0.17 (0.12)[B] 0.032[C] 0.028[D]	0.08 (0.02)[B]
Azelaic	0.18822	1251	202.1	0.18 (0.18)[A] 0.039[D]	-
Malonic	0.10406	1616	79.34	0.02 (0.02)[A] 0.045[E]	-
Pimelic	0.16017	1281	161.18	0.08 (0.08)[A] 0.23 (0.08)[B]	0.24 (0.04)[B]
Suberic	0.17419	1272	181.64	0.1 (0.1)[A] 0.05[X]	-
Succinic	0.11809	1566	99.8	0.125 (0.125)[A] 0.15 (0.07)[B] 0.075[D] 0.045[E]	0.07 (0.02)[B]

*: See Appendix B for calculation
**: Absolute uncertainty in values is provided in brackets where available. Values obtained from temperature-dependent expressions were taken to two significant figures at 50°C.
***: Literature values presented here; α of unity used in base model calculations.
[A]: Bilde 2003
[B]: Saleh 2009
[C]: Riipinen 2007, from temperature-dependent equation
[D]: Yaws 2003, from temperature-dependent equation
[E]: Hyvärinen 2006, from temperature-dependent equation
[X]: For suberic, half of Bilde value to assess sensitivity

Other studies that employ a kinetic model for evaporation in a TD make various assumptions regarding the aerosol diffusion coefficient. When considering specific aerosol, the HBS formula is often employed using available Lennard-Jones parameters [e.g. Bilde 2003]. A generic diffusion coefficient is often prescribed in the investigation of more complex mixtures or to generalize instrument conditions [e.g. Cappa and Jimenez 2010; Fuentes and McFiggans, 2012]. While the effect of diffusivity on aerosol volatilization is not being explicitly investigated in this study, the instrument model is

structured such that the incorporation of different representations to assess model sensitivity would be a trivial task.

The Fuchs-Sutugin non-continuum correction factor in equation (1) is defined as [Seinfeld and Pandis, 2006, Fuchs and Sutugin 1971]

$$\phi = \frac{0.75\alpha(1+\mathrm{Kn})}{\mathrm{Kn}^2+\mathrm{Kn}+0.283\mathrm{Kn}\alpha+0.75\alpha} \quad (5)$$

where $\frac{2\lambda_{AB}}{D_p}$ is the Knudsen number (Kn), and the mean free path, λ_{AB}, of the volatilizing compound (A) in air (B) is defined as $\lambda_{AB} = \frac{3D_{AB}}{\bar{c}_A}$, where $\bar{c}_A$ is the thermal molecular speed of the gas $\bar{c}_A = \left(\frac{8RT}{\pi M_A}\right)^{1/2}$ and α is the accommodation coefficient (the evaporation coefficient, if only volatilization occurs).

Equation (1) is integrated to determine the diameter of aerosol particles when they exit the heating section of the TD. This is done by initializing the particle size to the DMA-observed inlet conditions and then utilizing a differential equation solver, DVODE (Variable-coefficient Ordinary Differential Equation solver) [Brown 1989]. Each step in the integration is forward in time, as determined by the streamline velocity and spatial extent of the discretized finite volume cell. A new temperature is obtained at each point along the flow per propagation of the aerosol through the instrument. This causes a change in P_∞^o based on the prescribed reference volatility parameters which drives the aerosol volatilization along each streamline. The volume-weighted average of the final diameters exiting each streamline of the heating section is taken as the modeled outlet diameter, D_{pm}, and is calculated as

$$D_{pm} = \overline{D}_{p,v} = \frac{\int_0^{R_{TD}} D_p u_z r\, dr}{\int_0^{R_{TD}} u_z r\, dr} \quad (6)$$

where u_z represents the velocity along the streamline, r is the radial distance from the centerline with R_{TD} as the TD inner radius, and D_p is the particle diameter at the end of each streamline. The model output diameters, along with the observed aerosol diameters, are utilized in the optimization routine to retrieve estimates of volatility parameters.

The evaporation module was also generalized to treat mixtures of components by treating them as an ideal mixture following Raoult's law and determining the aerosol volatilization by the combined effect of each component. This approach, separating the aerosol mixture into multiple bins with specific properties, can be generalized as a form of the VBS as described in the introduction [Donahue et al. 2006].

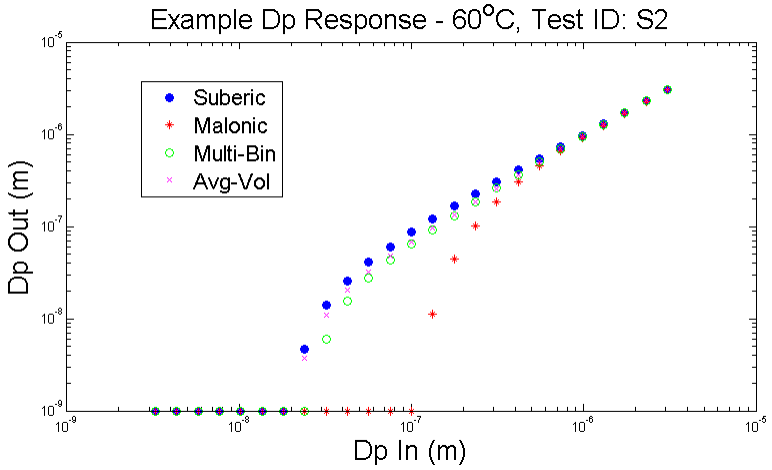

Figure 11: Example model response of a multicomponent simulation

An example is presented in Figure 11. Model results from runs using literature data for suberic and malonic acids were used to generate the single component response, which is plotted against the response of a mixture of equal parts by mass of the two components.

A simpler approximation of the expected aerosol response is also plotted (purple x). It is the diameter associated with the average volume of the two single component final diameters. This figure shows that the model is qualitatively consistent with the expected behavior of an ideal mixture of two components, with results similar to those obtained by Cappa [2010] where a model mixture of components with different volatilities were investigated.

2.1.3 Parameter Optimization

Optimization of the parameters used in the evaporation model is accomplished through the use of an iterative optimization algorithm, specifically the Levenberg-Marquardt curve fitting method as deployed in the International Mathematical and Statistical Library subroutine ZXSSQ (Ver. 6/1/1982) [IMSL]. Essentially, the model output diameters were calculated for a given set of initial conditions and volatility parameters. The model response was then compared against measured data, and a finite-difference Jacobian of the volatility parameters was calculated. Several iterations were then needed for the parameters to converge to those that satisfied the minimization of the differences between the model response and measured data.

Laboratory data was collected for each single component aerosol consisting of the upstream DMA-corrected inlet diameters ($D_{p,in}$) and associated outlet mode diameters ($D_{p,out}$) from the SMPS after the TD at three different temperature settings, T_{set}, with consistent flow rate settings, Q_{set}, of 1 LPM. Given that five values of $D_{p,in}$ were used for each set of measurements, a maximum of fifteen independent observations were available for each single component aerosol. However given the limitations of the measured outlet

size distributions, not all values of $D_{p,out}$ were used. The determination of the appropriate $D_{p,out}$ to be used in the model fitting is discussed further in the results.

Defining independent observations as unique combinations of $D_{p,in,}$ $T_{set,}$and Q_{set} for a particular aerosol provides a set of M equations, one for each observation, with N independent parameters – the aerosol properties ($\vec{x}^N$) chosen to be fitted to the data. Any number of independent parameters (N) for a particular single component aerosol can be estimated as long as $N \leq M$; though it would be preferable for the system to be overdetermined such that $N < M$ to obtain a robust parameter fit (i.e. least squares regression).

For the purposes of this study, the reference vapor pressure at 298K and enthalpy change are chosen to be optimized for the single component aerosol (N = 2), while other variables are defined using literature values. While it is possible to increase N provided a large enough value of M, doing so decreases the confidence of the fit and increases sensitivity to the initial condition used in the iterative scheme. Furthermore, decreasing the number of observations used (lowering M) also increases the likelihood of multiple minima due to fewer constraints. Thus the more observations fit to the least number of parameters provides the most robust parameter estimates. This was observed by using various initial conditions in the optimization scheme to fit the lab data to the model. The combinations consist of four decadally-spaced values of saturation vapor pressure from 10^{-4} to 10^{-7} Pa and three evenly-spaced values of enthalpy change spanning the range of reported literature values (9 to 19 kJ mol^{-1}, see table in appendix C), yielding twelve separate sets of initial conditions in total.

The Levenberg-Marquardt algorithm is an unconstrained optimization method which necessitated the use of variable transformation to avoid the occurrence of unphysical negative results. The enthalpy change was also scaled to be of the same magnitude as the saturation vapor pressure. The variable transformation was a simple squaring of the parameters estimated by the optimization routine:

$$\vec{x}^N = \left(\vec{P}^N\right)^2 \tag{7}$$

where $\vec{P}^N$ are the parameters fit to the model by ZXSSQ. This variable transformation is taken into consideration later in the results discussion and uncertainty analysis.

2.2 Data Collection

Volatility of samples in the laboratory was inferred through measured changes in the aerosol size using a VTDMA procedure [Orsini et al., 1998; Rader and McMurry, 1986]. Aerosol were first generated by atomization of prepared aqueous solutions containing organic solute below the solubility limit in order to avoid atomization of undissolved solute and were then passed through two silica gel diffusion dryers to remove the solvent water. Prior to being size-selected by a DMA, the aerosol charge distribution was equilibrated by a Kr-85 neutralizer, providing an approximately monodisperse – in terms of electrical mobility – aerosol sample at the diameter corresponding to the DMA voltage setting. The sample line was then diluted and split to a condensation particle counter (CPC) and a three-way valve just upstream of the TD. The valve can be controlled to either send the sample through the TD or through a bypass line; an identical valve was located downstream of the TD, operating in series to prohibit backflow. Downstream of the TD, the size distribution of the aerosol leaving the TD or bypass line was measured with an SMPS.

The voltage on the upstream DMA, alternation of the TD/bypass valve, and temperature setpoint of the TD was automated by LabVIEW™ virtual instruments (VIs) [National Instruments]. The separate DMA control VI and TD control VI schedules were synchronized with each other and with aerosol instrument manager (AIM) software to collect SMPS distributions corresponding to particular inlet size and TD setpoint conditions. Three TD samples were collected for each T_{set} and inlet diameter, and three corresponding bypass observations were made by alternating the three-way valve. Each full SMPS scan was integrated over approximately two minutes while also providing time between groups of measurements for the TD temperature to equilibrate. The DMA sheath to aerosol flow ratio was maintained at 10:1 with a sample flow of 1 LPM. TD setpoint temperatures chosen for the experiments were 40, 50, and 60^{o}C. DMA setpoint diameters chosen for the experiments were 0 (as a control), 60, 80, 100, 120, and 140 nanometers; however, the actual diameter selection varied based on the true voltage of the size-selecting DMA. A statistical correction was applied to those selected diameters based on a comparison to the DMA used in the downstream SMPS measurements to account for biases between the two. This was chosen as an alternative to using the bypass SMPS diameters as a representation of the inlet diameter; although, these values are presented in Figures 12-18 for a qualitative interpretation. These modifications are reflected in the final reported inlet diameters which were used to initialize the model. The outlet diameters are taken as the mode diameter of the observed size distributions (average of three samples).

The volatilities of six straight-chain dicarboxylic acids were investigated using this technique. Available literature saturation vapor pressure data suggest the volatilities

of these compounds may range several orders of magnitude (see Appendix C). Chemical sources and reported mass purities were as follows: adipic acid, Fisher Scientific, 99%; azelaic acid, City Chemical LLC, 98%; malonic acid, Fisher Scientific, reagent grade; pimelic acid, Acros Organics, 99%; suberic acid, Acros Organic, 99%; succinic acid, Acros Organics, 99%. Chemicals were used as received with no further purification steps. Atomized solutions were made with deionized water generated from a reverse osmosis filtration method. Example SMPS distributions for each reagent, inlet diameter, and temperature setting are shown in the Figures 12-18 to illustrate the volatilization of the aerosol samples. Note that two sets of measurements were made for malonic acid. Two additional compounds were investigated in the work: glutamic and phthalic acid. Results are not presented for these compounds however because they did not volatilize at any of the three temperature setpoints – the observed size change was within the measurement uncertainty for all measurements. They were, of course, expected to be less volatile compounds due to their additional structural complexity versus the straight-chain dicarboxylic acids. Glutamic acid is an amino acid containing an additional functional group, and phthalic acid is an aromatic dicarboxylic acid. Since no volatilization was observed, no parameters could be retrieved. This is an expected limitation of investigating volatility at relatively low temperatures and should be considered in the planning of future experiments. Data interpretation is discussed further in the results section, and tabulated data (average mode diameters) for each organic acid are provided in Appendix D.

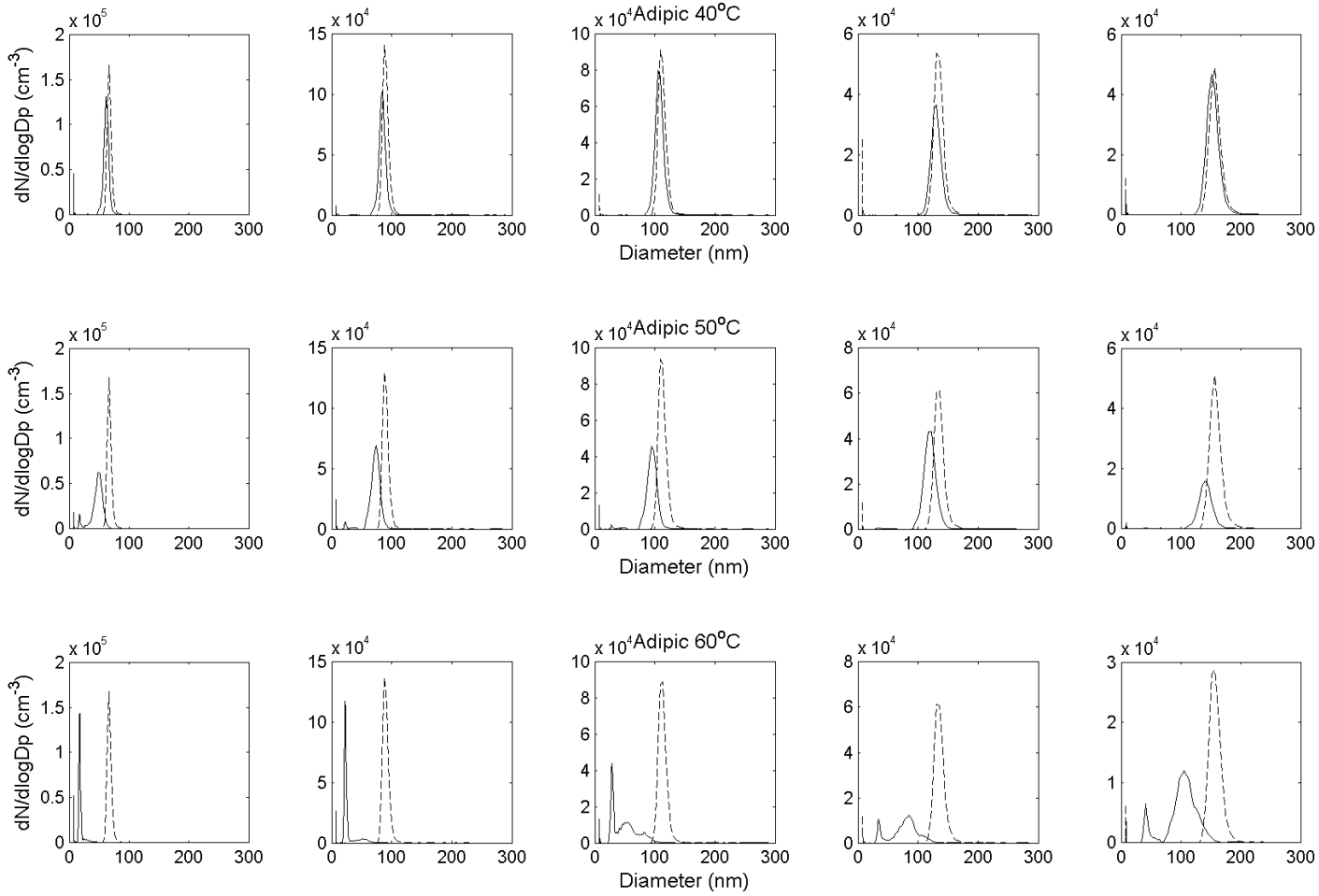

Figure 12: Size distribution changes from SMPS measurements, bypass (dashed) and TD (solid), for adipic acid

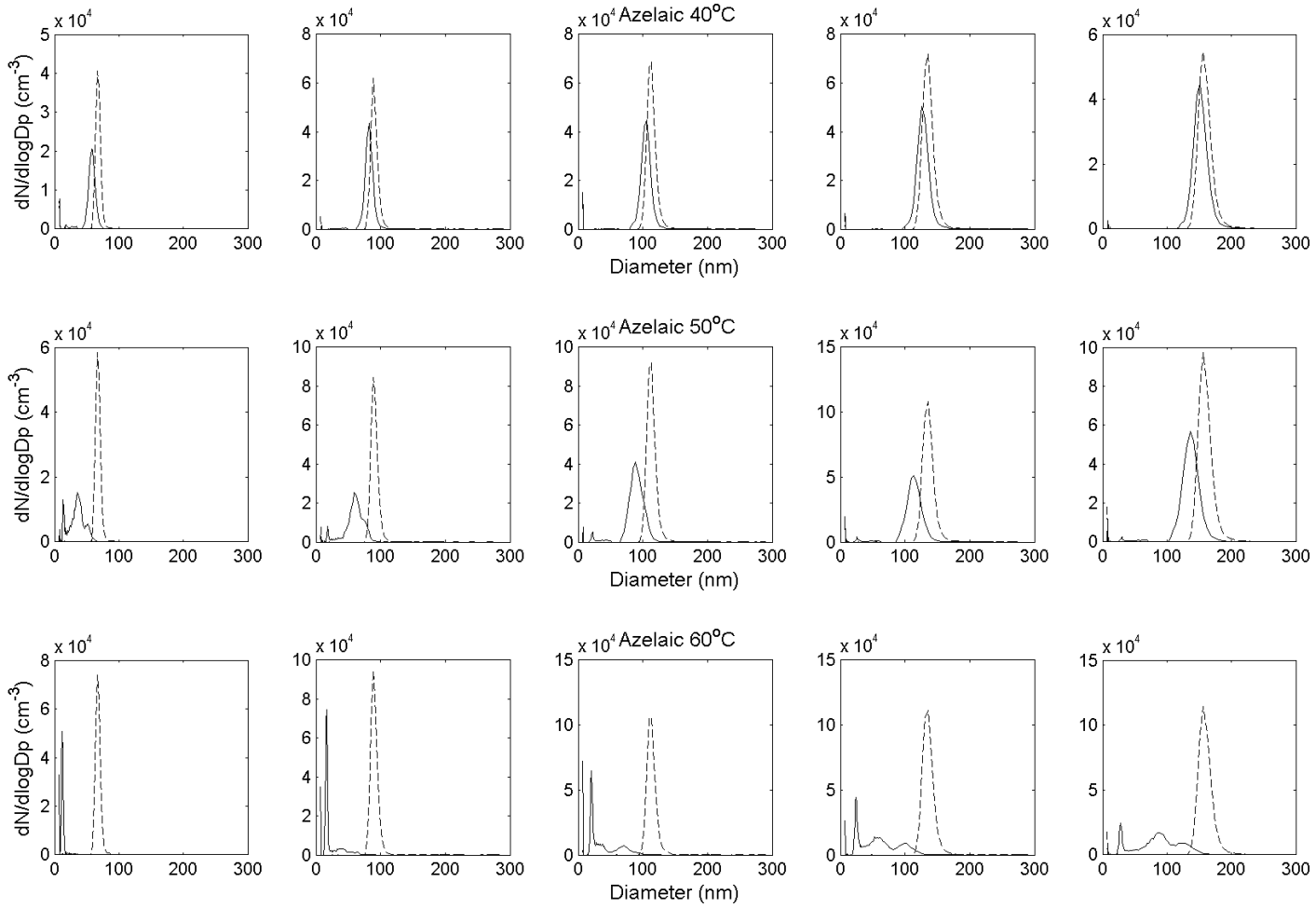

Figure 13: Size distribution changes from SMPS measurements, bypass (dashed) and TD (solid), for azelaic acid

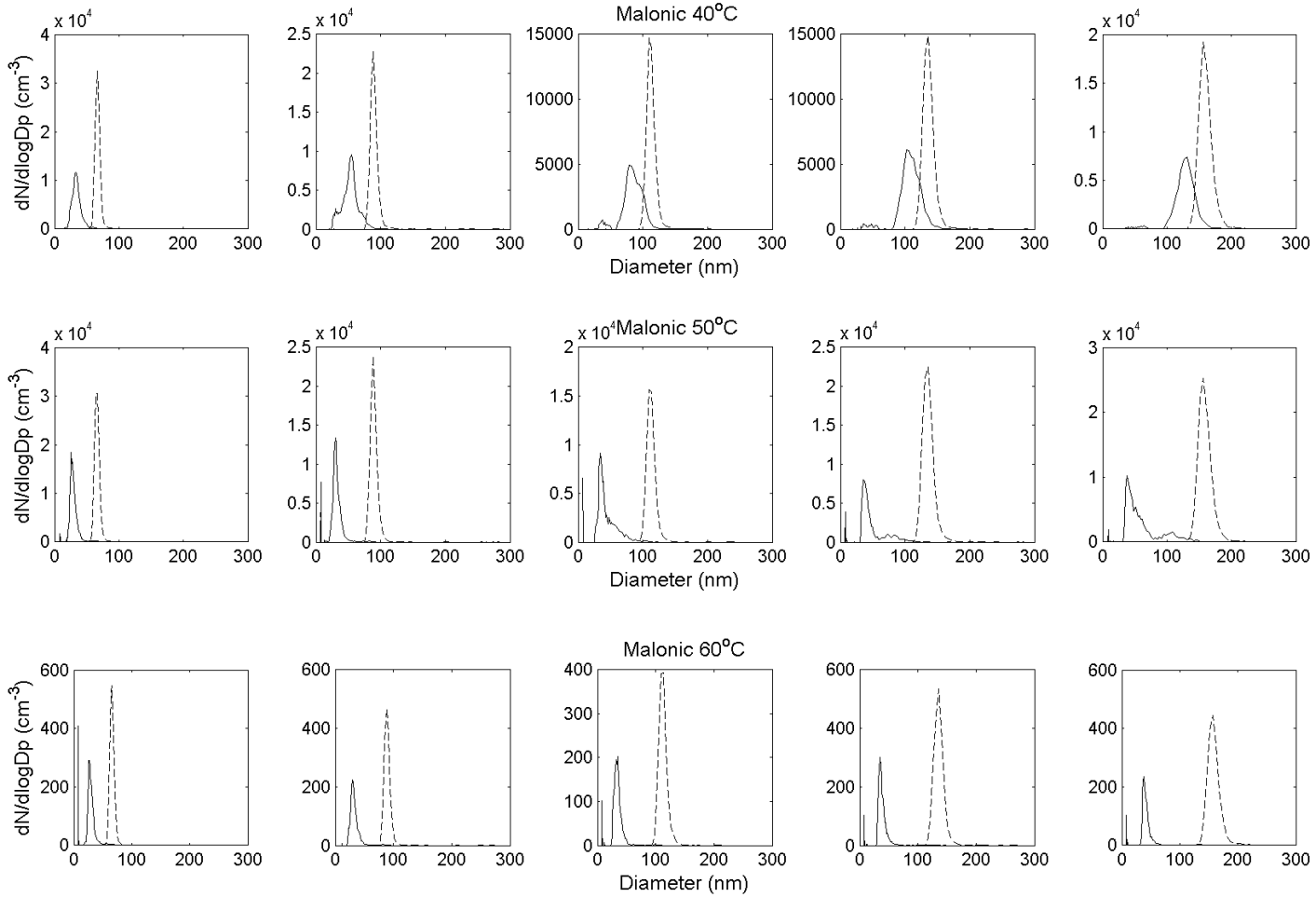

Figure 14: Size distribution changes from SMPS measurements, bypass (dashed) and TD (solid), for malonic acid – set #1

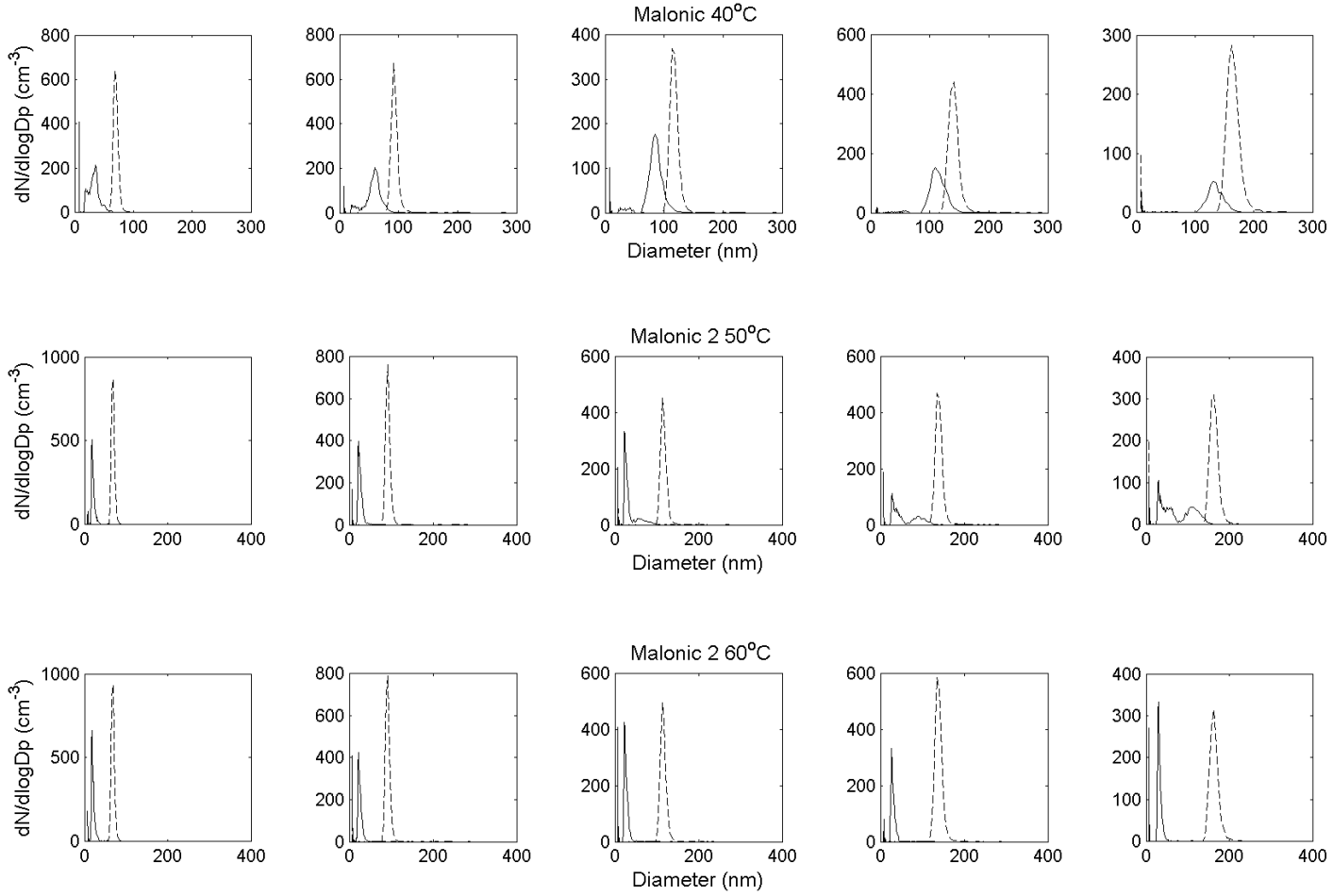

Figure 15: Size distribution changes from SMPS measurements, bypass (dashed) and TD (solid), for malonic acid – set #2

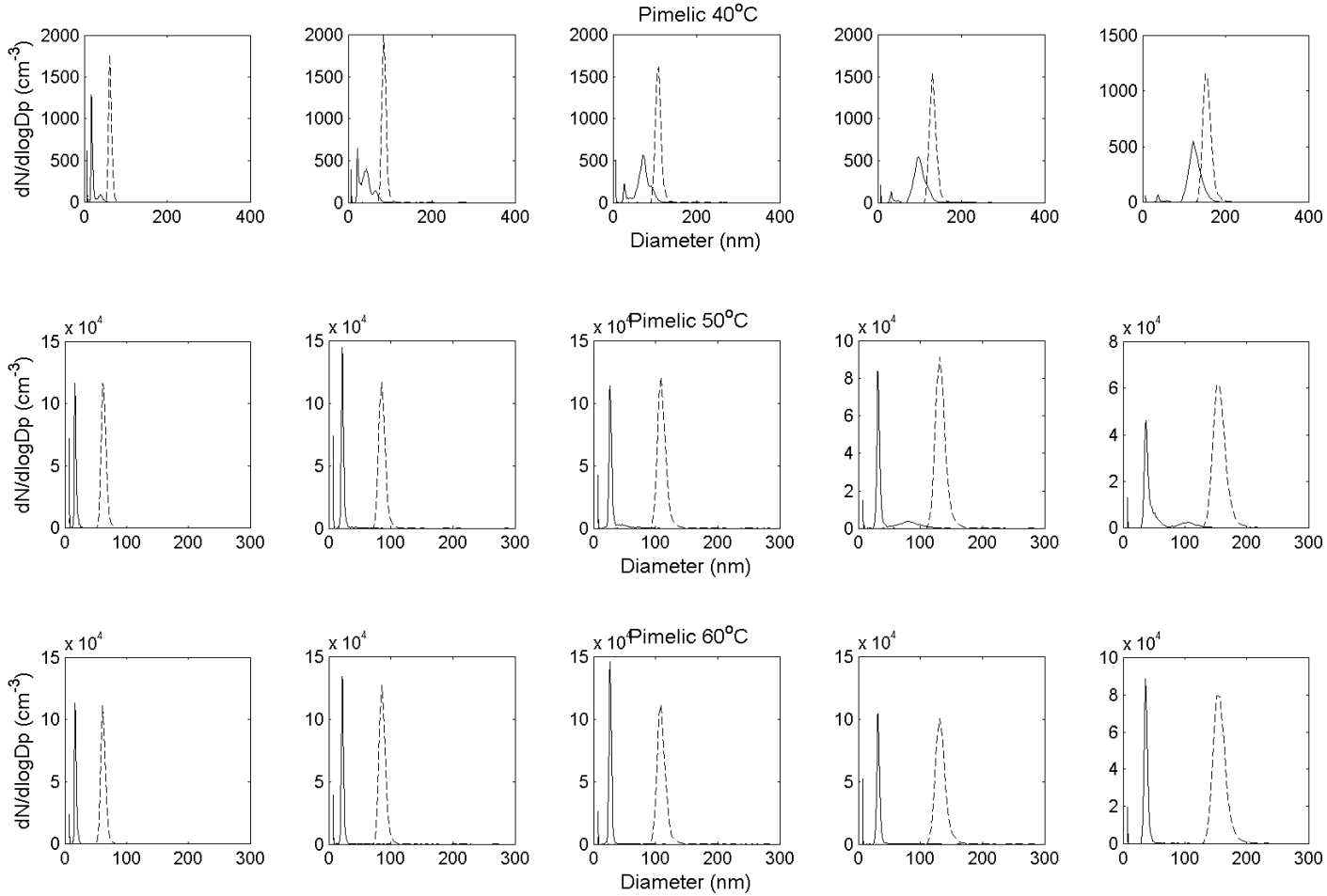

Figure 16: Size distribution changes from SMPS measurements, bypass (dashed) and TD (solid), for pimelic acid

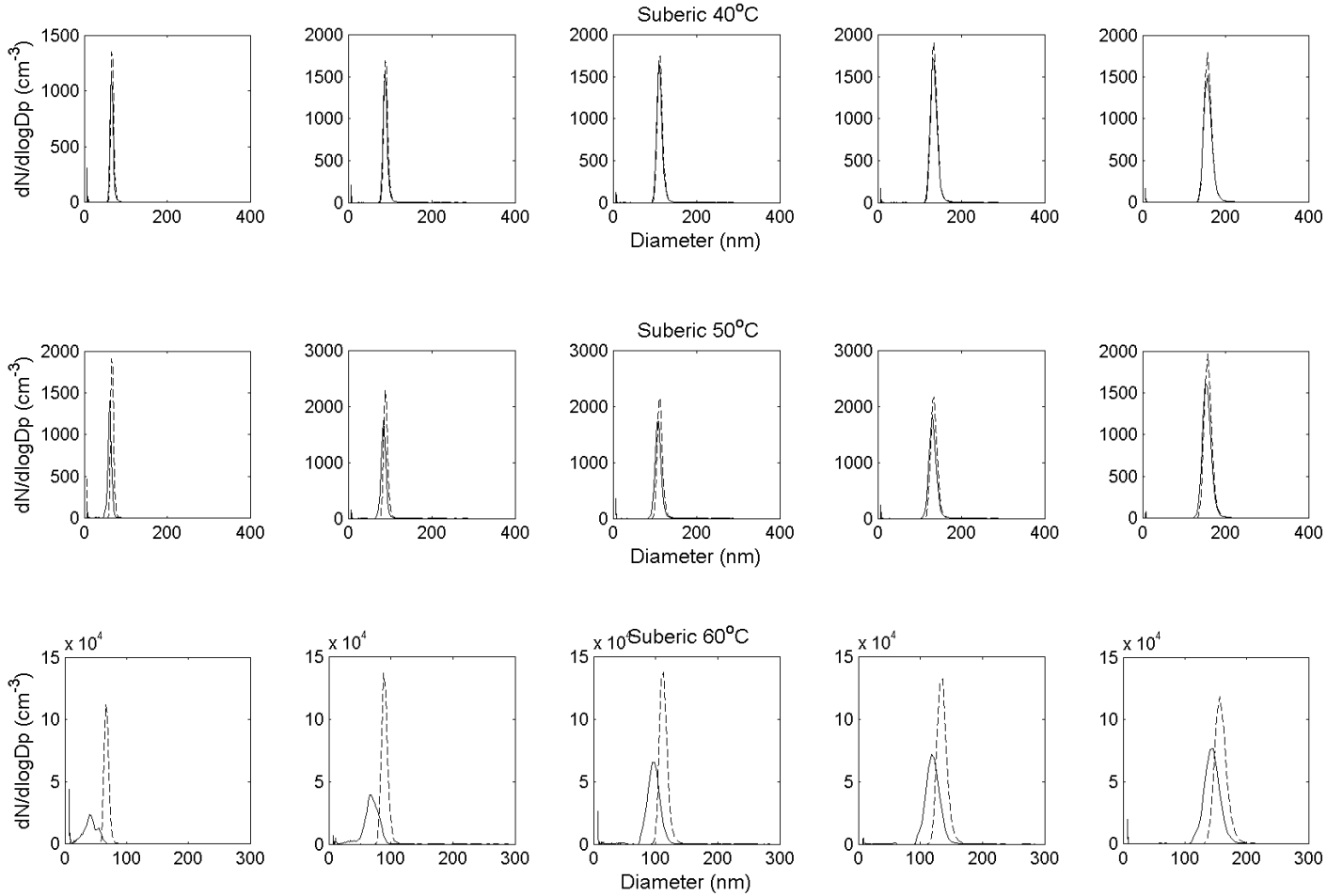

Figure 17: Size distribution changes from SMPS measurements, bypass (dashed) and TD (solid), for suberic acid

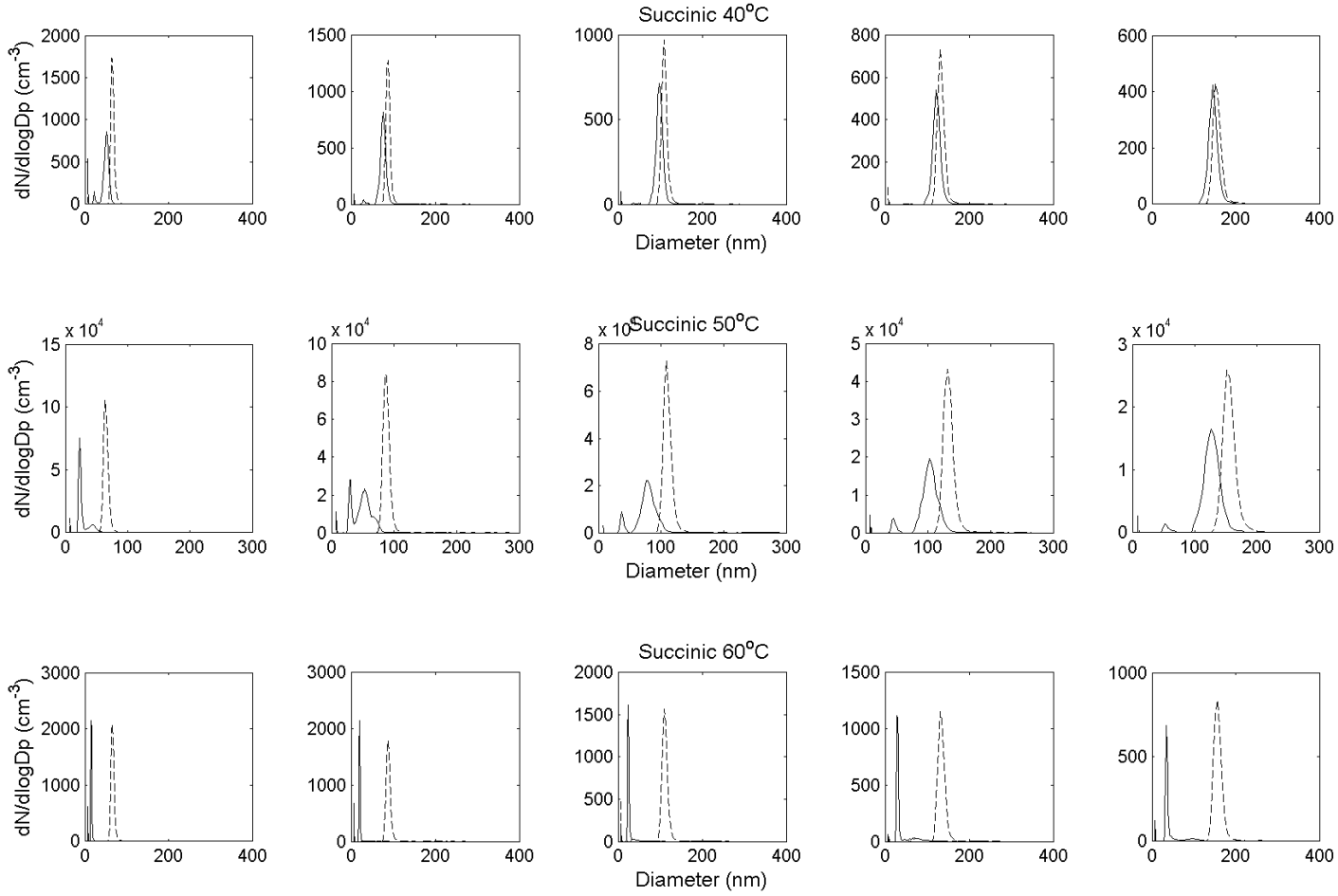

Figure 18: Size distribution changes from SMPS measurements, bypass (dashed) and TD (solid), for succinic acid.

CHAPTER 3: RESULTS

3.1 Effects of Model Flow Variation on Volatility

To compare the evaporation module response to variations in the flow field, an arbitrary selection of aerosol characteristics was made. For reference, the properties used were taken from literature values for azelaic acid. A size distribution spanning a wide range of inlet diameters that encompass those of interest to this work was used to initialize the model for four different flow field conditions: the full calculation involving resolution of the velocity and temperature distribution in the model TD, and the partial calculation of just temperature diffusion through an ideal laminar flow – both at two settings of inlet temperature (293 and 298 K). The differences between the four simulations are illustrated by plotting the residuals of the model mean output diameter for the various inlet diameters against each other for each T_{set} in Figures 19-21. The left-hand plot in each set shows that increasing the inlet temperature tends to decrease the mean output diameter, but even at the 60^{o}C setpoint, this effect only decreases the average diameter by about 1 nanometer at most. Whereas the residual between the full and partial calculation indicates the full solution consistently produces aerosol larger than the partial solution, with residuals of greater magnitude than those associated with changes in the inlet temperature. The likely explanation for this result is that the increase in the axial velocity due to thermal expansion (see Figures 9 and 10) would reduce the residence time of the aerosol within the TD enough to keep them from volatilizing as much as they would in the ideal laminar flow. Greater values for the residuals between the flow calculations at the lower inlet temperature further support this idea, since there would be a larger

decrease in the aerosol residence time when compared against the ideal laminar flow velocity. The absolute values of these residuals are likely dependent upon the individual aerosol properties – meaning more volatile aerosol would experience more of an effect. However, the relative difference between the response associated with changes in inlet temperature and those associated with changes in the velocity of the flow should be the same for aerosol of varying volatility.

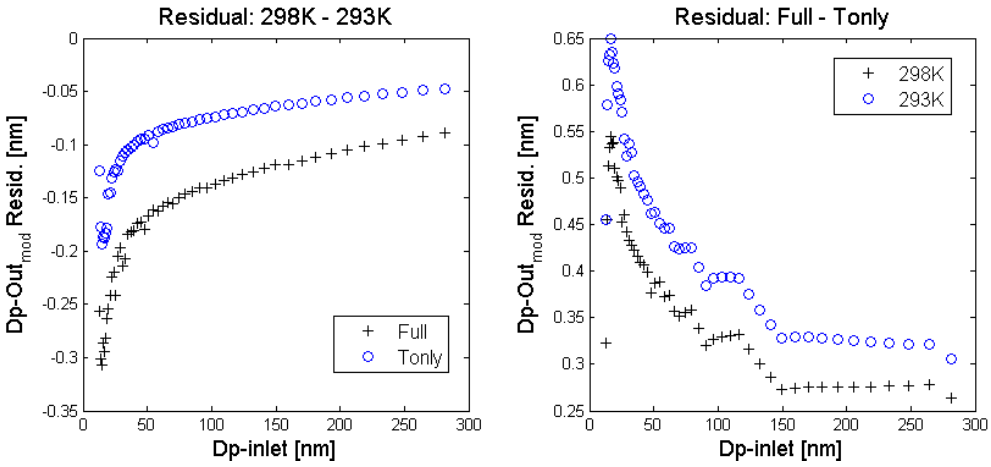

Figure 19: Volatilization sensitivity to flow variation at 40°C setpoint

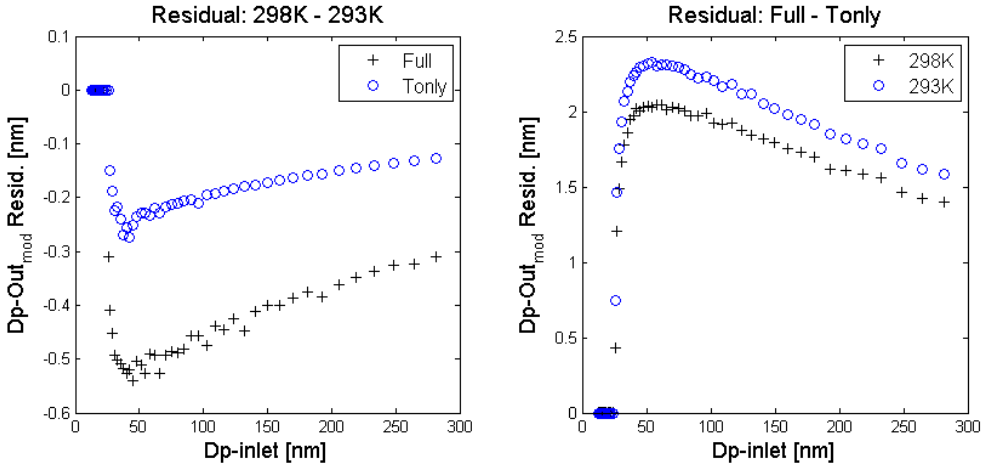

Figure 20: Volatilization sensitivity to flow variation at 50°C setpoint

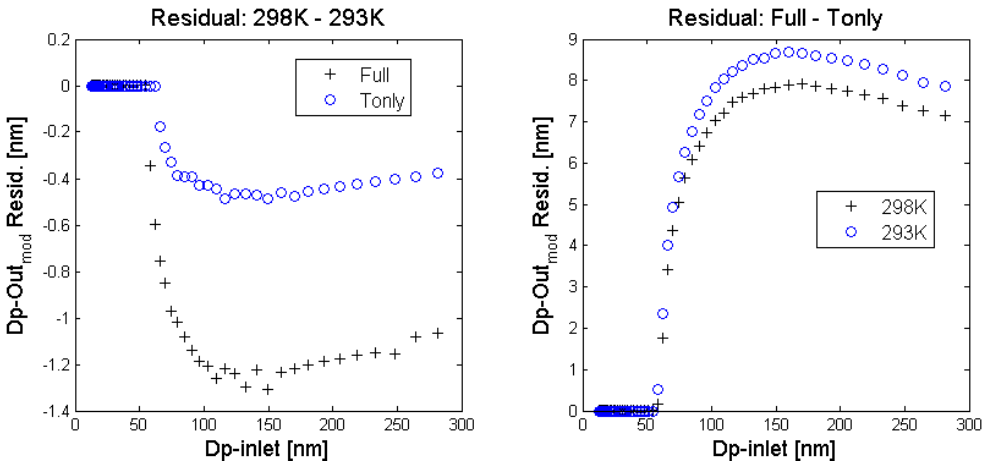

Figure 21: Volatilization sensitivity to flow variation at 60°C setpoint

Another way of visualizing the effects of flow field variations on the volatilization of model aerosol is to look at the response residuals of individual streamlines. Contour plots for the 40°C and 60°C setpoint streamline residuals are shown in Figures 22 and 23 to illustrate the non-uniformity of the aerosol response – likely representing the noise in the plots of the average diameter response in the previous figures. At lower setpoint temperatures (i.e. 40°C) outliers can be observed in the model response near the TD wall. Whereas there are otherwise minimal differences between the full and partial calculation evaporation module response, near the TD wall the full calculation result is much less than the partial calculation – a negative residual. This is likely due to the existence of a boundary layer in the full solution's flow where the velocity drops to near zero, increasing the residence time and thus the volatilization of the aerosol. At the higher T_{set}, this effect is not observed; rather, the expected result of a generally positive residual associated with the shorter residence times in the full calculation can be observed, with the maximum occurring near the margin of the volatilization range.

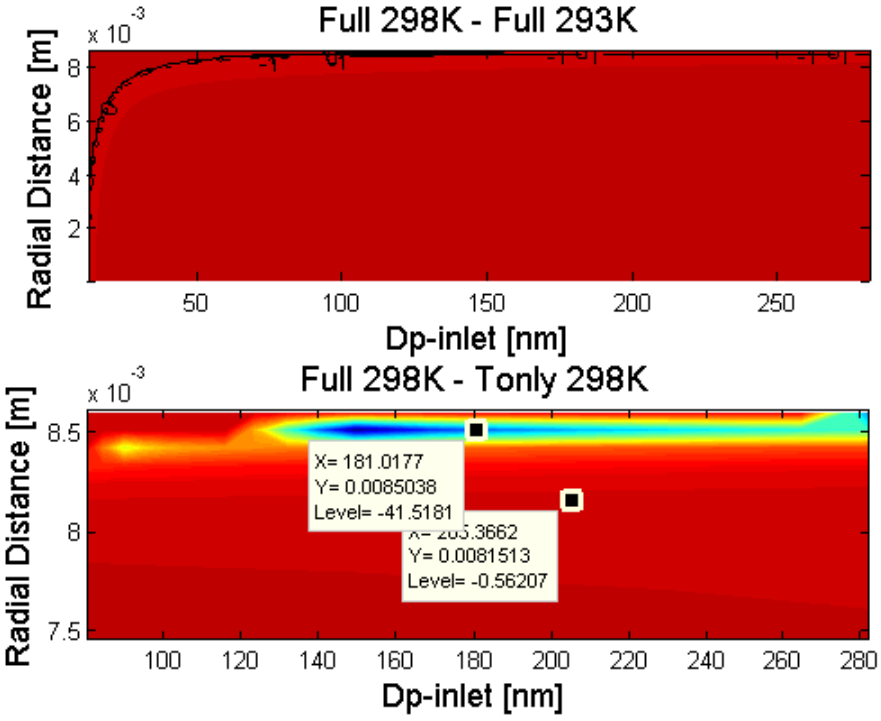

Figure 22: Streamline volatilization residuals for 40°C setpoint

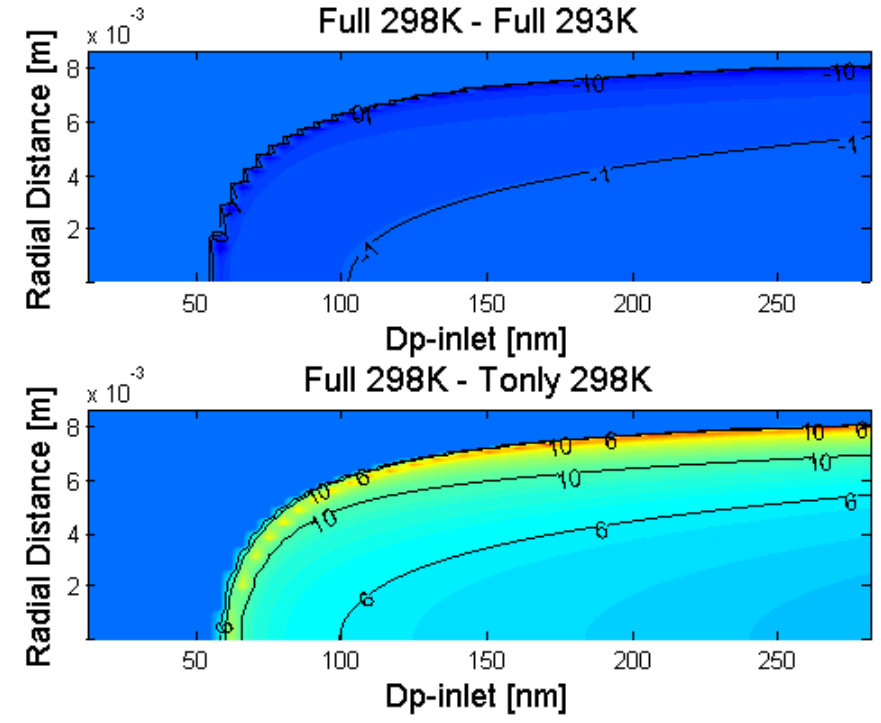

Figure 23: Streamline volatilization residuals for 60°C setpoint

Since the aerosol completely volatilizes near the wall in both the partial and full solution fields at the higher temperature setting, there are no outliers in the residual field near the TD wall. It should be noted that no colorbar is provided for Figures 22 and 23, but reference contours are labeled with units of nanometers; the upper subplots show the residuals for varying the inlet temperature and are clearly of much smaller magnitude.

3.2 Data Limitations & Quality Control

Through the course of analyzing changes in the size distributions after the volatilization of aerosol within the TD, multiple modes were observed in the SMPS size distributions (Figures 12-18). Subsets of the data were unimodal, bimodal, and trimodal. This is concerning for several reasons. First, there must be assurance that there is one particular outlet diameter of an aerosol of fixed composition from the TD for any given inlet diameter. Otherwise, the use of laboratory measurements to retrieve model parameters for the given aerosol would be mired in the arbitrary selection of one out of various mode diameters, as the occurrence of multiple modes is in direct contrast with the expectation of the mass transfer employed in the numerical model. A secondary concern regards the future use of the method in retrieving volatility parameters for ambient measurements. This requires a full understanding of the TD instrument response, including irregularities associated with measurement limitations and design constraints. In order to obtain multiple modes, there must be additional processes aside from volatilization, even considering the radial dependence on aerosol lifetimes associated with a laminar flow – where a mere broadening of the size distribution is expected. Alternatively, errors in the measurement of the size distribution could play a role. The investigation into these processes provided an opportunity to further characterize the instrument response and

validate data collection techniques. In the end, two simple explanations were determined to explain the existence of the additional modes. The presence of residual non-volatile cores from the impurities in the provided samples explained the lower of the three modes in the size distributions. The double-charging of particles explained the presence of the highest of the three modes.

In a previous study [Bilde et al., 2001], the effect of impurities was acknowledged to be of importance for aerosol of 150 nm diameter or less, and the authors accounted for this by adjusting their experiments to exclude analysis of aerosol in that size range. However, measurements were desired in this particular size range to support measurements of aerosol hygroscopicity downstream of the TD [Cerully et al., In Prep.], so the use of larger inlet diameters was not an option. Non-volatile residual components of the chemical sample could leave behind a residual particle in situations where the aerosol would have otherwise completely evaporated or when the fraction of the aerosol population following the streamlines nearer the TD wall completely volatilized while the fraction nearer the centerline remains. The latter situation would result in the presence of a second mode to the left (smaller mode diameter) of the true signal.

The residual diameter, $D_{p,resid}$, was calculated by taking the fractional mass purity (p) reported for provided samples and calculating the equivalent-volume sphere that would have the same mass considering the initial diameter, $D_{p,in}$, the density of the compound (ρ), and an assumption about the density of the residual matter (ρ_{resid}).

$$D_{p,resid} = \left(D_{p,in}^3 \frac{\rho}{\rho_{resid}} (1 - p) \right)^{1/3} \tag{8}$$

The effect of a large density difference between the organic compound and residual matter would, however, confound this estimation. Residual diameters are calculated two

ways: assuming the residual density is the same as the organic compound and assuming it has the density of NaCl salt (denser). The uncertainty in the inlet diameter measurement is also propagated through the estimate of the residual diameter. These calculated values were compared with the $D_{p,out}$ values of the lowest diameter mode from the SMPS data. Figures 24-30 illustrate the comparison for each organic acid at the reported mass purities. The data appear to fall into two distinct sets of points in the figures: one close to the 1:1: line and another well underneath it. For malonic acid, the mass purity was assumed to be 98%. Particular observations were considered to be contaminated with noise from the non-volatile core signal when values of $D_{p,out}$ and $D_{p,resid}$ fall near the 1:1 line, within the uncertainty range. Data that was just outside of agreement were also considered to be contaminated since the exact density of the residual was unknown and were omitted from the model parameter optimization along with those that were within the understood uncertainty range.

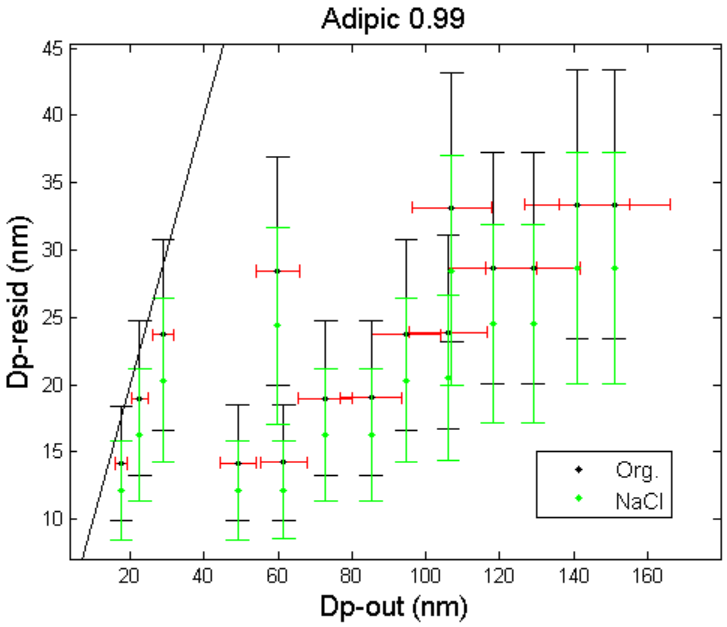

Figure 24: Residual diameter comparison for adipic acid

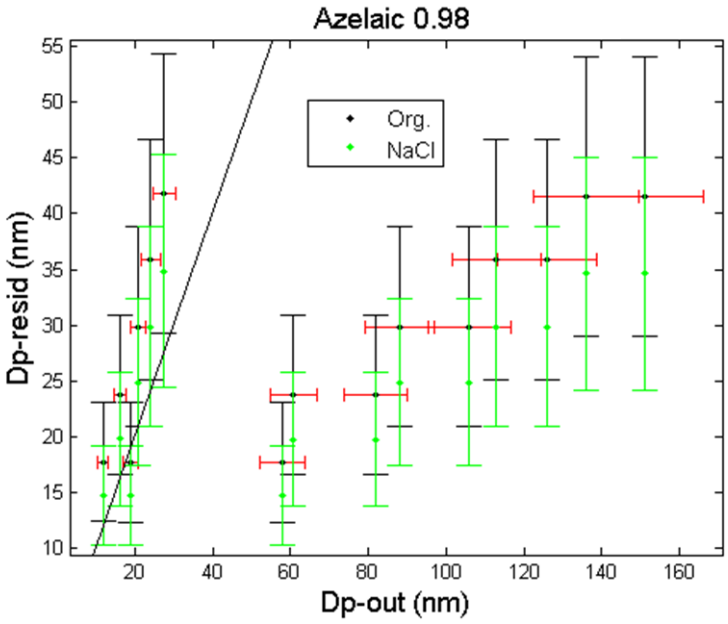

Figure 25: Residual diameter comparison for azelaic acid

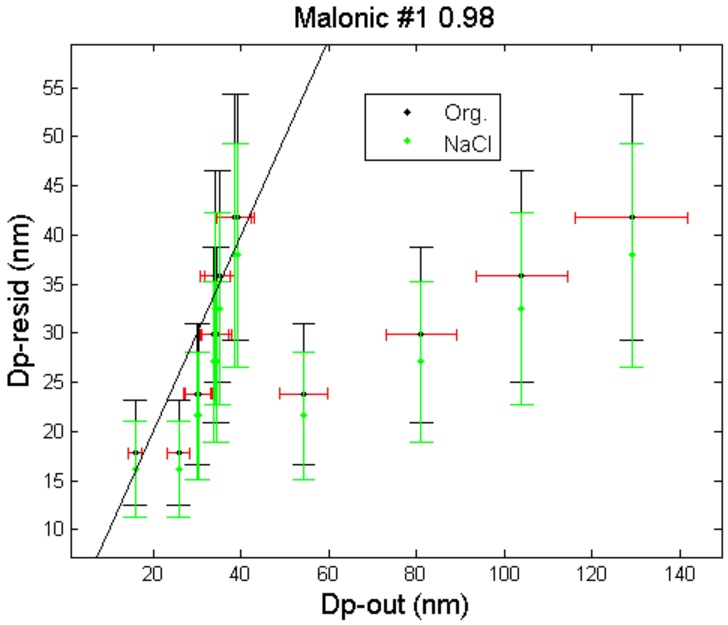

Figure 26: Residual diameter comparison for malonic acid (#1)

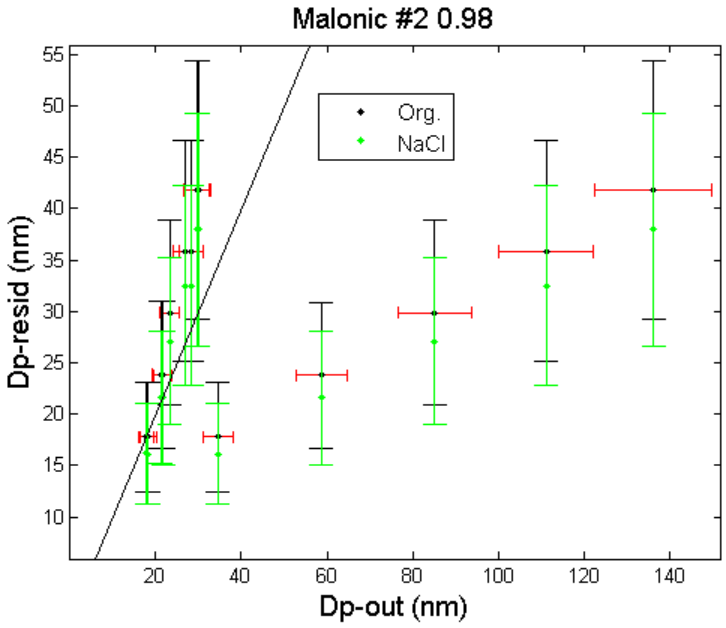

Figure 27: Residual diameter comparison for malonic acid (#2)

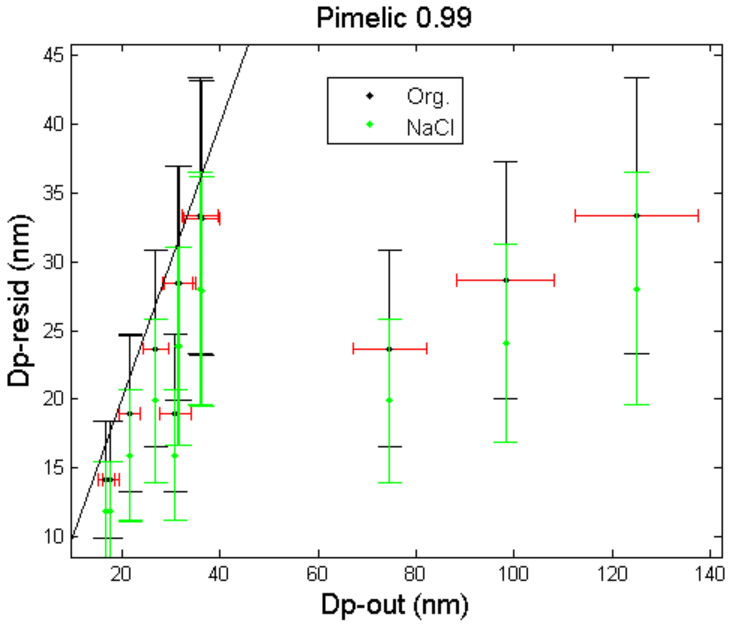

Figure 28: Residual diameter comparison for pimelic acid

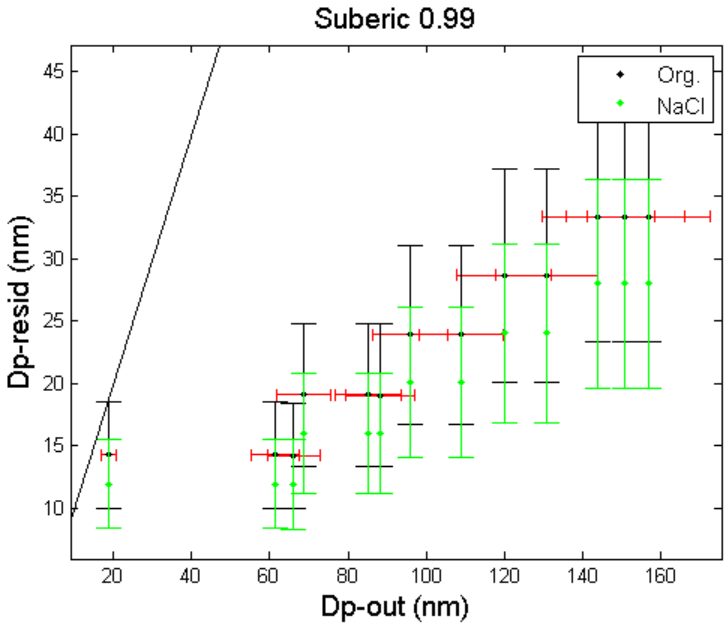

Figure 29: Residual diameter comparison for suberic acid

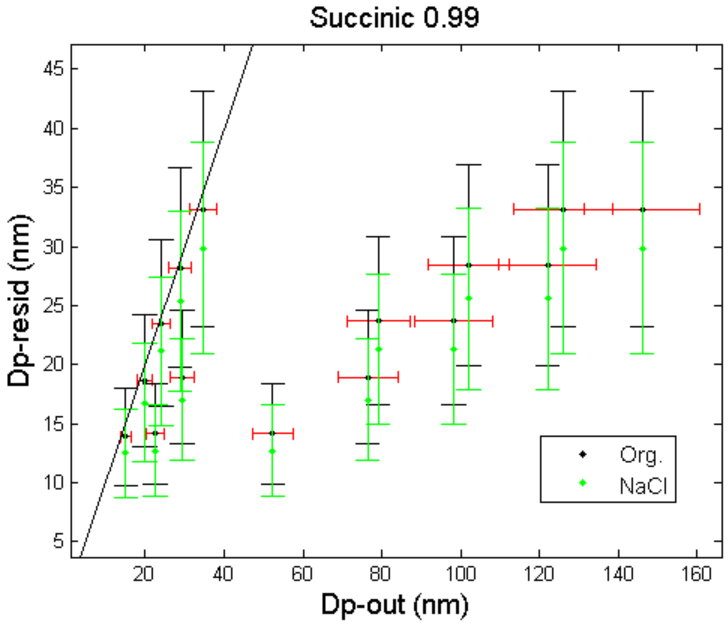

Figure 30: Residual diameter comparison for succinic acid

The presence of double-charged particles appeared to explain the largest diameter mode in the observed tri-modal distributions. Considering a spherical aerosol with the same electrical mobility as the single-charged aerosol with $D_{p,in}$, the double-charged diameter, $D_{p,2x}$, is equal to

$$D_{p,2x} = \frac{2C_c(D_{p,2x})}{1C_c(D_{p,in})} D_{p,in} \quad (9)$$

where $C_c = 1 + \frac{2\lambda}{D_p}\left[1.257 + 0.4\exp\left(-\frac{1.1D_p}{2\lambda}\right)\right]$ is the Cunningham slip correction factor [Seinfeld and Pandis, 2006]. The dependence on particle diameter requires the calculation to be iterated until it converges to a particular value of $D_{p,2x}$. Equation (9) is obtained by setting the following expression for electrical mobility, Z_e, to be equal for the two sets of conditions: q = 1, D_p = $D_{p,in}$ and q = 2, D_p = $D_{p,2x}$, where q is the number of elementary charges on a particle of size D_p and the expression for the electrical mobility is

$$Z_e = \frac{qC_c}{3\pi\mu D_p} \quad (10)$$

with μ defined as the kinematic viscosity of air. These $D_{p,2x}$ were then used to initialize the evaporation module using the same volatility parameters estimating from the fitting of the middle modes, and the results ($D_{p,out}$) were compared against the largest diameter mode in the observed size distribution in the Figures 31-34. This was done in all cases, whether or not a trimodal distribution was observed. Suberic and pimelic acids were not included in this analysis because neither was observed to exhibit trimodal size distributions in the measurements, likely because suberic was too nonvolatile and pimelic was too volatile. The figures indicate that the model predicted outlet diameter for the double-charged particles agrees with the largest diameter mode, regardless of the number of modes observed; thus, the third (leftmost) mode was not observed when the outlet

diameters for the double-charged and single-charged inlet diameters were similar. This explanation is consistent with the laboratory setup where the particle charge distribution was re-equilibrated at the second DMA downstream of the TD. The double-charged particles would not be observed in the SMPS size distributions otherwise since their electric mobility would be greater than that of singly-charged particles with the same geometric diameter.

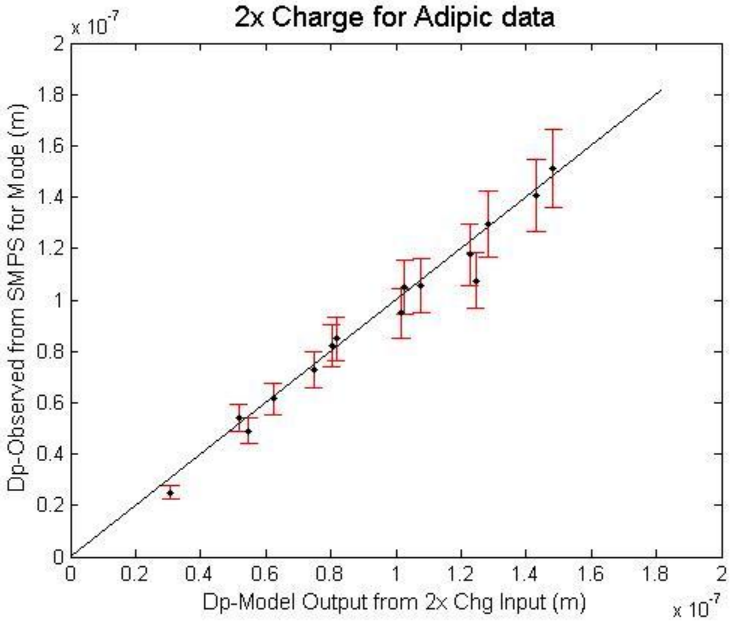

Figure 31: Expected double-charged response versus observations for adipic acid

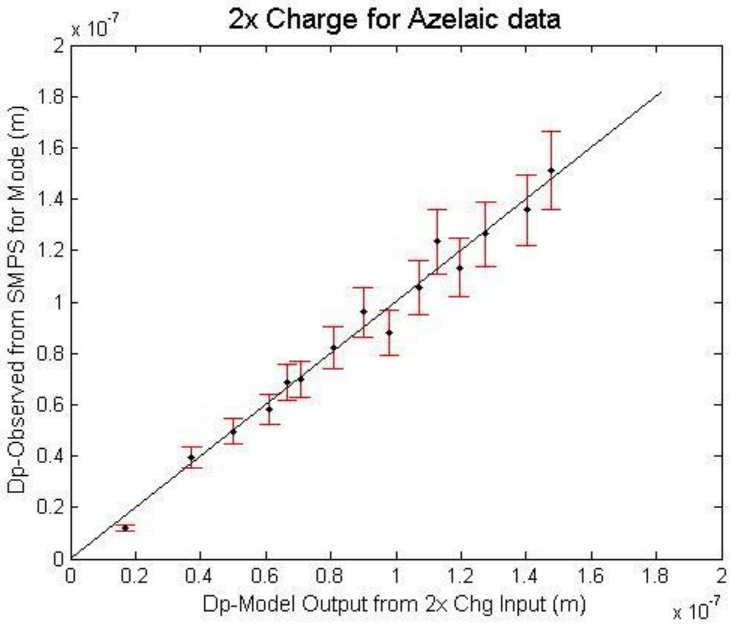

Figure 32: Expected double-charged response versus observations for azelaic acid

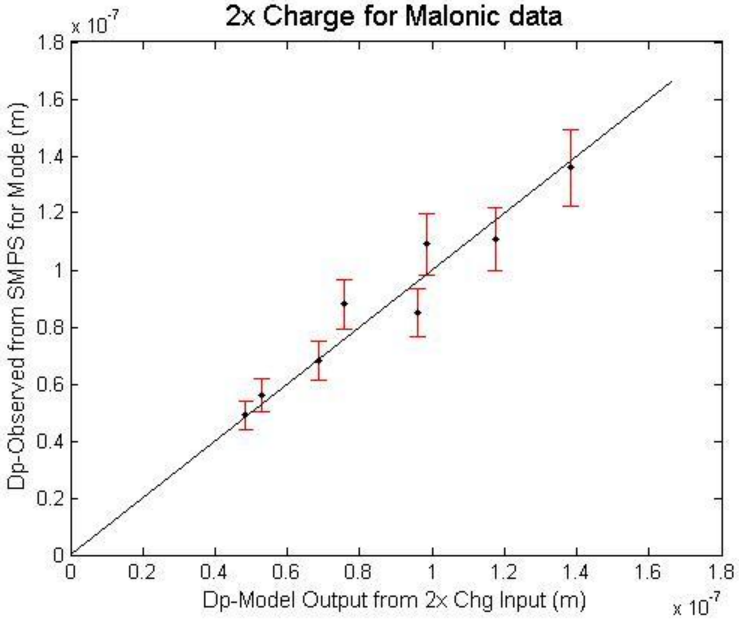

Figure 33: Expected double-charged response versus observations for malonic acid

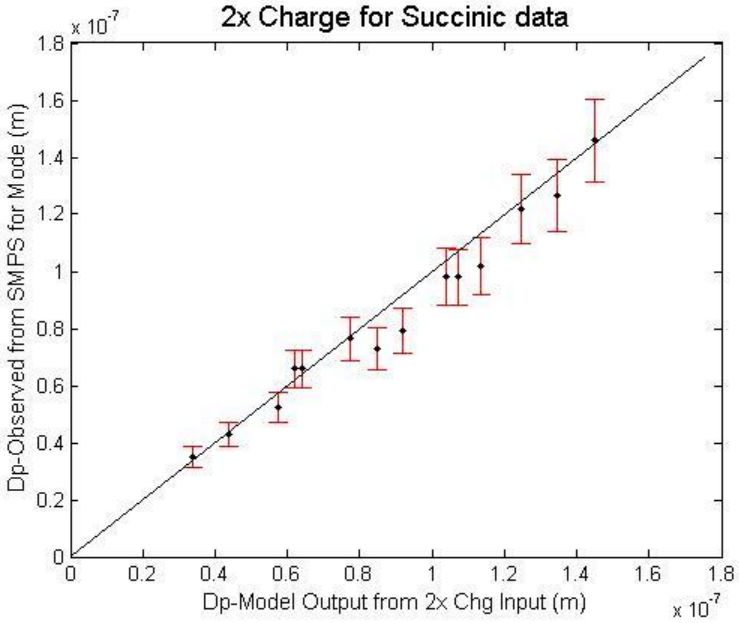

Figure 34: Expected double-charged response versus observations for succinic acid

Another observable effect of the aerosol charge re-equilibration at the downstream DMA is the reduction in observed particle number concentration due to a selection of a further subset of the original aerosol passed through the TD. These reductions are much greater than that expected to be caused by particle losses within the TD alone. Volatilization of aerosol is also not likely to be the cause either as even with relatively nonvolatile aerosol the reduction in number concentration is observed (see size distribution Figures 12-18, specifically those of suberic acid and others at 40^{o}C). For this reason, average number concentrations recorded by the CPC upstream of the TD were used when such data was needed to avoid potential bias in the number concentrations inferred from the downstream SMPS, considering negligible particle losses in the TD determined by theoretical calculations [Cerully et al., In Prep.].

Taking the data adjustments described above into consideration, the graphical results of the model fitting of volatility parameters are presented below in Figures 35-41. Solid curves represent the model fitting at the optimized parameters. The dashed curves represent the upper and lower limits on the aerosol volatility parameters. Starred points represent measured data that was fitted, and open circles represent raw data that was either adjusted to the starred points through selection of a different mode or completely left out of the model fitting. For some compounds, there are additional or absent curves. Adipic has an additional set of blue curves that were drawn from a different set of optimized volatility parameters as a sensitivity test. Pimelic has an additional set of blue curves that were drawn from another set of optimized parameters to illustrate the problem of multiple minima in the optimization routine for retrievals with limited data. Suberic lacks an upper bound on the uncertainty range of its volatility because the uncertainty range was so large that it included negative values for vapor pressure.

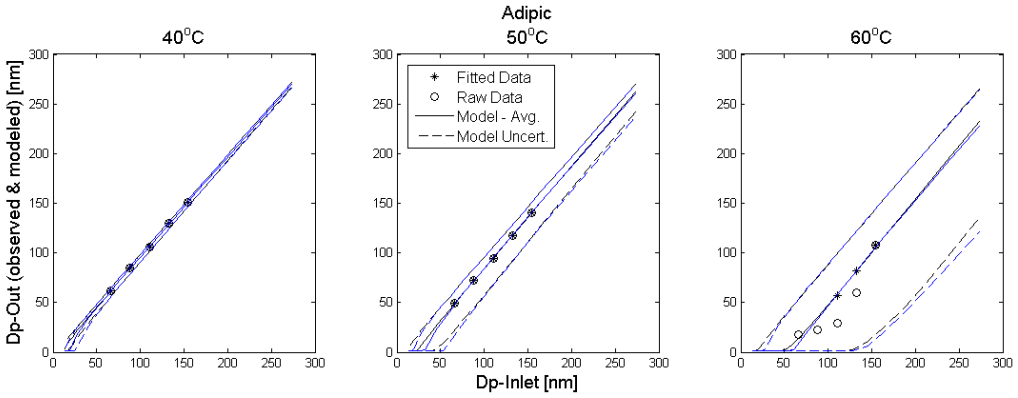

Figure 35: Model fitting visualization for adipic acid

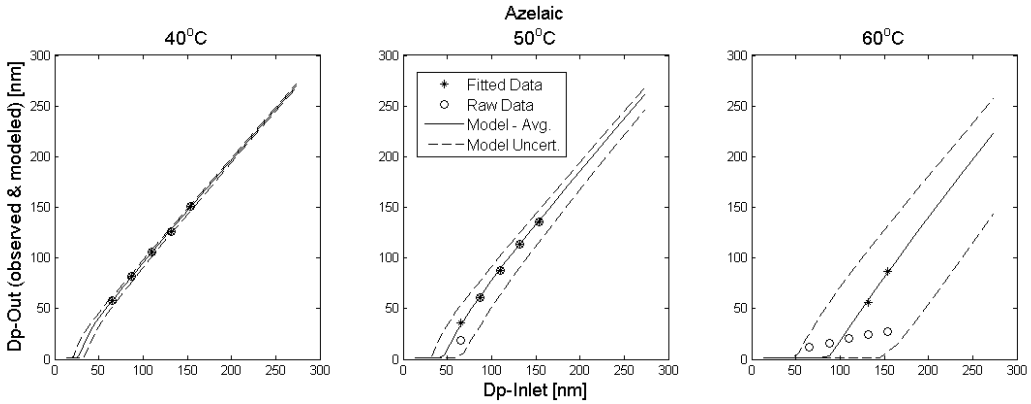

Figure 36: Model fitting visualization for azelaic acid

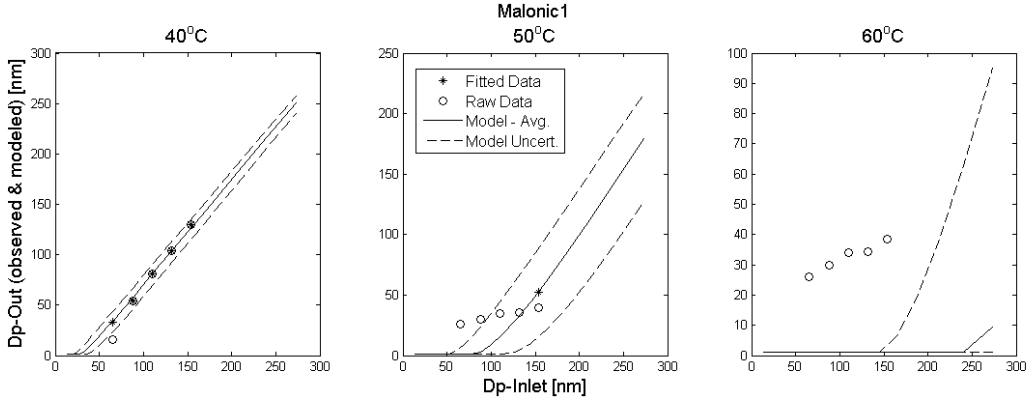

Figure 37: Model fitting visualization for malonic acid (#1)

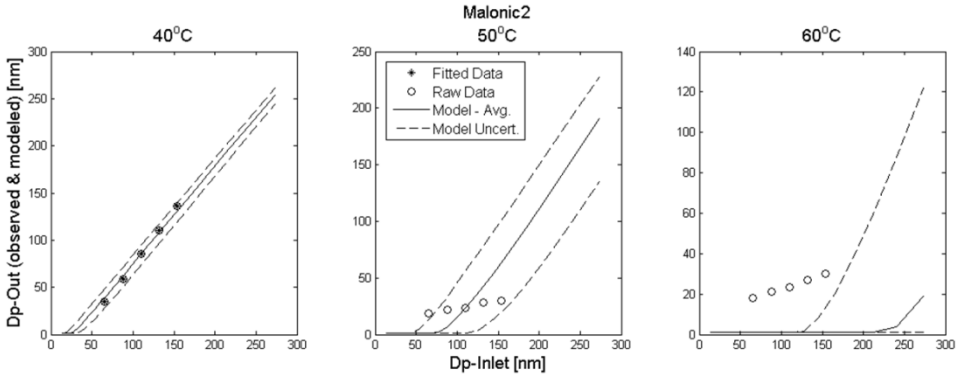

Figure 38: Model fitting visualization for malonic acid (#2)

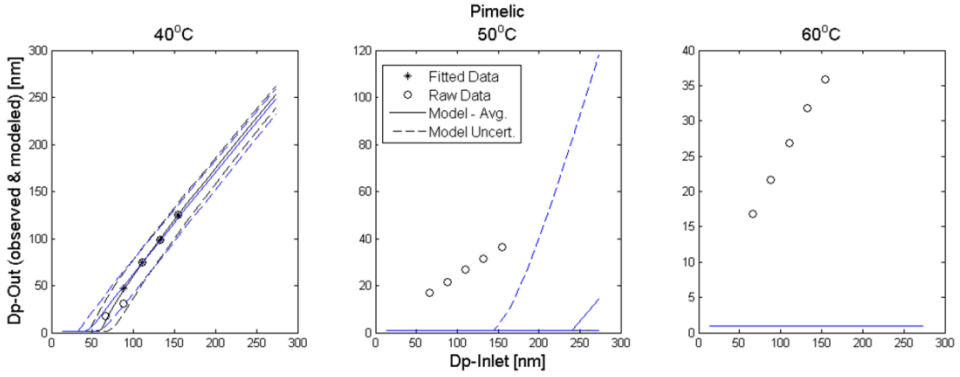

Figure 39: Model fitting visualization for pimelic acid

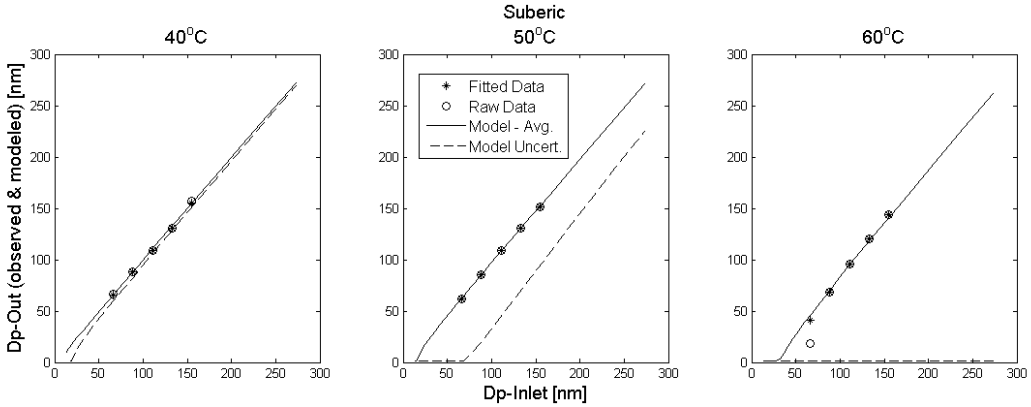

Figure 40: Model fitting visualization for suberic acid

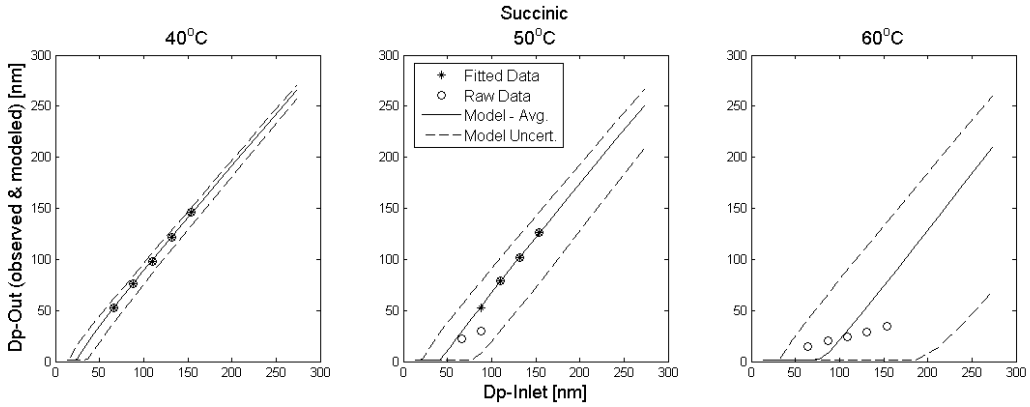

Figure 41: Model fitting visualization for succinic acid

Further assumptions were made regarding the phase, shape and morphology of the aerosol in order to model the volatilization in this way. Aerosols were assumed to be spherical with diameter equivalent to that associated with the DMA-selected electrical mobility. This assumption can be corrected for irregularly-shaped aerosol by the inclusion of a shape factor and is not necessary for liquid aerosol as they form spherical droplets. For instance, a previous study found solid (crystalline) adipic and azelaic acid aerosol to have dynamic shape factors between 1.05 and 1.1 [Saleh et al., 2010], suggesting an overestimation of particle diameter when assuming spherical geometry for solid (crystalline) aerosol near 10%. While this estimated shape factor is based on scanning electron microscope imagery for two particular dicarboxylic acids and is therefore not necessarily representative of all OA, it provides a possible range of systematic correction to the DMA sizing if the aerosol phase is known to be that of a crystalline solid. While aerosol in this study is generated from atomization of an unsaturated solution at room temperature, it is unlikely that the dried aerosol have a crystalline morphology considering the short drying time – no dilution volume is used prior to the silica diffusion driers (as in Saleh et al. [2010]). Another study [Salo et al. 2010] indicated that solvent inclusions are unlikely to be present in aerosol generated with a drying setup similar to Saleh [2010], although noting that the hysteresis of aerosol deliquescence and efflorescence regarding ambient relative humidity allows for the possibility of having externally mixed liquid and solid phase aerosol. Calculations of volatility parameters for separate measurements suggested that this occurred for pimelic acid in their experiments. With these results in mind, the aerosol generated in this study can likely be considered either an amorphous solid or supercooled melt of the atomized

compound since they were generated well below typical melting temperatures of dicarboxylic acids.

3.3 Single-Component Volatility Parameters

Volatility parameters and uncertainty ranges for each investigated organic acid were obtained through the use of the ZXSSQ optimization routine coupled with the instrument model. The optimization routine minimizes the returned residuals of a black-box function which in this case the evaporation module where the cost function, *C*, was defined as

$$C = \sum_{i=1}^{M}(Y_i)^2 = \sum_{i=1}^{M}\left(D_{p,out,i} - D_{pm,i}\right)^2 \quad (11)$$

where *Y* is the residuals vector of length M returned by the evaporation module each time it is called by the optimization routine. The algorithm calculates the finite-difference Jacobian, matrix *J*, at each point in the optimization space as it minimizes *C*. It is defined as the partial derivative of each term of the cost function with respect to perturbations in each parameter in the optimization space.

$$J_{ij} = \frac{\partial Y_i}{\partial P_j} = \frac{\Delta\left(D_{p,out,i} - D_{pm,i}\right)}{\Delta P_j} = \frac{\Delta D_{p,out,i}}{\Delta P_j} - \frac{\Delta D_{pm,i}}{\Delta P_j} \quad (12)$$

During the parameter optimization, $\Delta D_{p,out,i} = 0$ since $D_{p,out}$ is essentially a constant and unaffected by model parameters, and J_{ij} can be interpreted as the D_{pm} sensitivity to variations in the optimization-space parameter, P_j. Once the parameter optimization is complete, ZXSSQ returns the final values of the parameters, and the physical parameters (*x*) are obtained by performing the variable transformation described in equation (7). The volatility parameter uncertainty ranges are determined by first applying *J* to calculate ΔP_j for a given variation in inlet diameter, $\Delta D_{p,out,i}$, which is taken to represent the uncertainty in the measured outlet diameters. In this case, $\Delta D_{pm,i} = 0$ and the relationship to *J* is defined as

$$\Delta P_{ij} = \frac{\Delta D_{p,out,i}}{J_{ij}} \quad (13)$$

The relative uncertainties in the transformed and untransformed variables are proportional in accordance with equation (7), such that

$$2\left(\frac{\Delta P_j}{P_j}\right) = \frac{\Delta x_j}{x_j} \quad (14)$$

The volatility parameter uncertainty can then be calculated as

$$\Delta x_{ij} = \frac{2\Delta D_{p,out,i} x_j}{P_j J_{ij}} = \frac{2\Delta D_{p,out,i} P_j}{J_{ij}} \quad (15)$$

As may be inferred from the notation, this provides a measure of uncertainty for each observed outlet diameter. These values can span a few orders of magnitude, as changes in diameter at lower temperature setpoints translate into larger changes in the volatility parameters and the uncertainty in the diameter measurement is proportional to the measured size. Therefore a weighted average of the measures of uncertainty is taken as

$$\Delta x_j = \frac{\sum_i^M w_i \Delta x_{ij}}{\sum_i^M w_i} \quad (16)$$

with weights defined as the observed diameter change experienced by the aerosol:

$$w_i = \left(D_{p,in,i} - D_{p,out,i}\right) \quad (17)$$

In such a way, volatility parameters and associated uncertainty ranges were obtained by initiating the ZXSSQ-coupled model with twelve sets of initial conditions as described previously. In the model optimizations, the literature value used for the interfacial energy was varied to assess the sensitivity of the retrieved parameters. The accommodation/evaporation coefficient was assumed to be unity by default but was also varied to literature values in Table 1 where available. The results for each compound that presented the least residuals against the laboratory data out of the various initial

conditions were taken as the model fits and are presented in Table 2. These results are also presented graphically in a comparison against literature data in Figures 42-47.

Results for adipic acid are presented in Figure 42. This figure and those subsequent compare the results from this study (cyan points with blue error bars) and those from the literature: red points and bars indicate data for vapor pressure and enthalpy of sublimation associated with vapor-solid equilibrium, and magenta points and bars indicate data for vapor pressure and enthalpy of vaporization associated with vapor-liquid equilibrium.

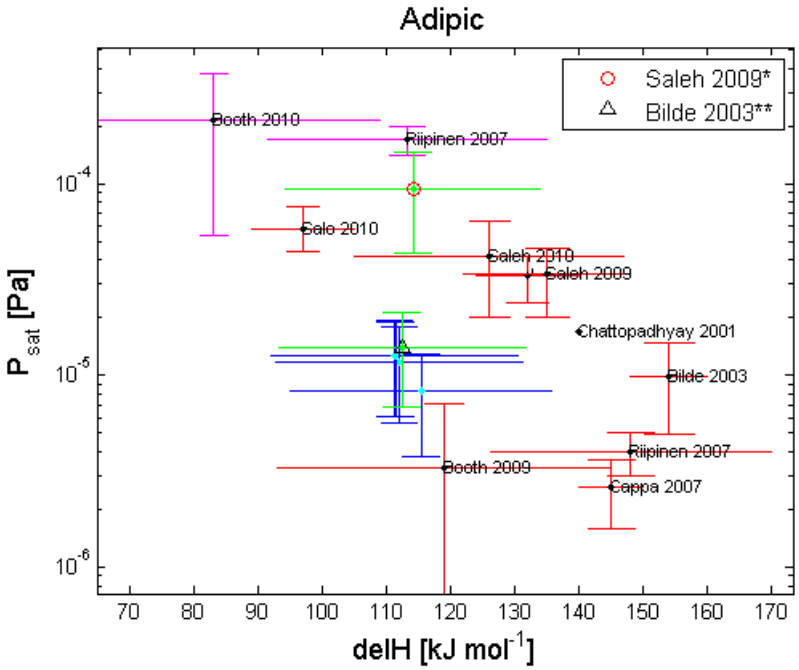

Figure 42: Literature comparison of volatility parameters for adipic acid

Points plotted with symbols indicated in the legend and green error bars correspond to sensitivity calculations where some additional factor was adjusted using the interfacial

energy from the specified source such that the result may be compared to the base case (one of the cyan/blue points). Table 2 gives more detail regarding the factors involved in the sensitivity calculations. Results for adipic acid indicate that perturbing the background saturation ratio does not appear to have much of an effect on the retrieved volatility parameter. Adjusting the accommodation/evaporation coefficient to the literature value produces a more dramatic change in the retrieved volatility parameters, but the result is not consistent with the corresponding reference [Saleh 2009].

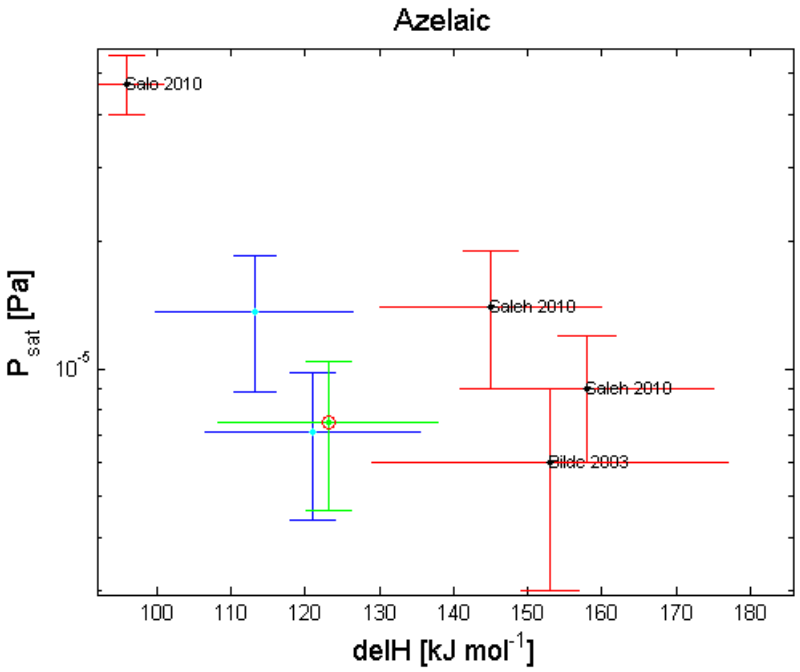

Figure 43: Literature comparison of volatility parameters for azelaic acid

For azelaic acid, changes in the interfacial energy resulted in larger volatility parameter changes than perturbing the background saturation ratio (note that Figure 43 is zoomed

in, omitting an outlier value from Cappa 2007). For malonic acid, the results for this work include data from the two separate samples (#1 and #2 – as they have been referred to so far) as well as the combination of both sets of data. This provides the spread of points that can be seen in Figure 44.

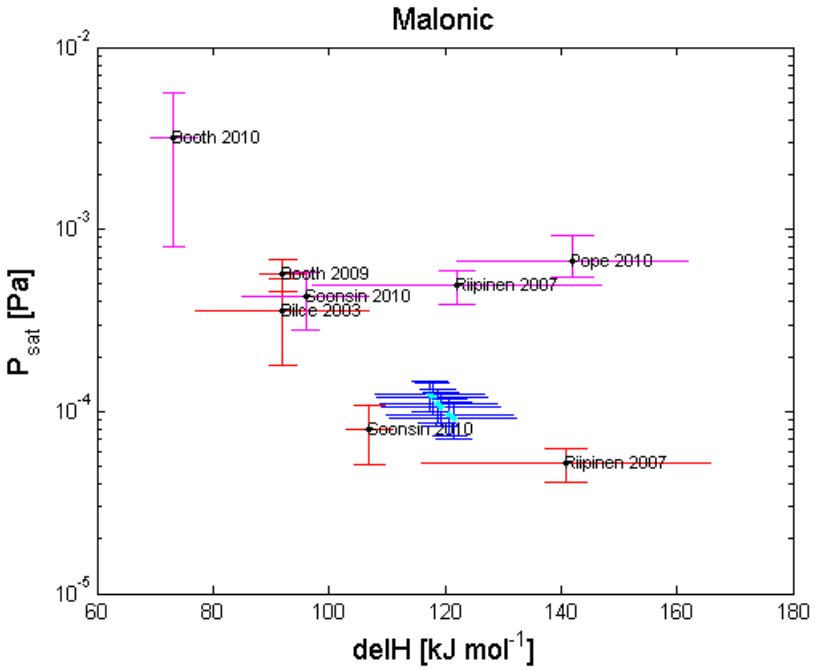

Figure 44: Literature comparison of volatility parameters for malonic acid

Table 2: Volatility parameters and uncertainty ranges obtained from model fits to laboratory data

	Interfacial Energy	P_{sat}(298K), Pa			ΔH, J			C*(298K)	
Adipic	**N m^{-1}**	**Max.**	**Min.**	**Avg.**	**Max.**	**Min.**	**Avg.**	**µg m^{-3}**	**% Uncert.**
Bilde 2003	0.06	1.8E-05	5.6E-06	1.2E-05	1.3E+05	9.3E+04	1.1E+05	0.691	52.10%
Riip 2007	0.032	1.9E-05	6.1E-06	1.3E-05	1.3E+05	9.2E+04	1.1E+05	0.744	51.78%
Saleh 2009	0.17	1.3E-05	3.8E-06	8.4E-06	1.4E+05	9.5E+04	1.2E+05	0.494	54.74%
Yaws 2003	0.028	1.9E-05	6.1E-06	1.3E-05	1.3E+05	9.2E+04	1.1E+05	0.751	51.97%
Saleh 2009*	0.17	1.5E-04	4.4E-05	9.4E-05	1.3E+05	9.4E+04	1.1E+05	5.569	53.61%
Bilde 2003**	0.06	2.1E-05	6.8E-06	1.4E-05	1.3E+05	9.3E+04	1.1E+05	0.830	51.63%
Azelaic									
Bilde 2003	0.18	9.8E-06	4.4E-06	7.1E-06	1.4E+05	1.1E+05	1.2E+05	0.541	38.19%
Yaws 2003	0.039	1.9E-05	8.8E-06	1.4E-05	1.3E+05	1.0E+05	1.1E+05	1.042	35.54%
Bilde 2003**	0.18	1.0E-05	4.6E-06	7.5E-06	1.4E+05	1.1E+05	1.2E+05	0.570	38.43%
Malonic 1									
Bilde 2003	0.02	1.5E-04	1.0E-04	1.2E-04	1.3E+05	1.1E+05	1.2E+05	5.199	19.39%
Hyvar. 2006	0.045	1.4E-04	9.5E-05	1.2E-04	1.3E+05	1.1E+05	1.2E+05	4.992	19.67%
Malonic 2									
Bilde 2003	0.02	1.2E-04	7.4E-05	9.6E-05	1.3E+05	1.1E+05	1.2E+05	4.039	23.09%
Hyvar. 2006	0.045	1.1E-04	7.1E-05	9.2E-05	1.3E+05	1.1E+05	1.2E+05	3.868	22.93%
Malonic C.									
Bilde 2003	0.02	1.3E-04	8.7E-05	1.1E-04	1.3E+05	1.1E+05	1.2E+05	4.634	21.09%
Hyvar. 2006	0.045	1.3E-04	8.3E-05	1.1E-04	1.3E+05	1.1E+05	1.2E+05	4.436	21.45%

Table 2 (continued)

Pimelic									
Bilde 2003	0.08	1.9E-05	1.1E-05	1.5E-05	2.2E+05	1.9E+05	2.1E+05	0.953	26.04%
Saleh 2009	0.23	2.3E-07	1.3E-07	1.8E-07	4.2E+05	3.9E+05	4.1E+05	0.012	26.77%
Saleh 2009*	0.23	1.7E-05	1.0E-05	1.4E-05	2.7E+05	2.4E+05	2.6E+05	0.877	26.41%
Suberic									
Bilde 2003	0.1	1.7E-06	-4.5E-07	6.0E-07	2.1E+05	8.0E+04	1.4E+05	0.043	173.9%
Other	0.05	1.8E-06	-4.8E-07	6.7E-07	2.1E+05	8.1E+04	1.5E+05	0.047	172.1%
Succinic									
Bilde 2003	0.125	8.9E-05	3.1E-05	6.0E-05	1.1E+05	7.1E+04	9.1E+04	2.868	47.82%
Saleh 2009	0.15	8.5E-05	3.0E-05	5.8E-05	1.1E+05	7.1E+04	9.1E+04	2.750	47.77%
Yaws 2003	0.075	9.7E-05	3.4E-05	6.5E-05	1.1E+05	7.0E+04	9.0E+04	3.115	47.72%
Hyvar. 2006	0.045	1.0E-04	3.6E-05	6.8E-05	1.1E+05	7.0E+04	9.0E+04	3.250	47.59%
Saleh 2009*	0.15	5.5E-04	1.6E-04	2.7E-04	1.2E+05	2.6E+04	1.0E+05	12.65	106.0%
Saleh 2009**	0.15	1.0E-04	3.6E-05	6.8E-05	1.1E+05	7.1E+04	9.2E+04	3.263	47.82%
Saleh 2009***	0.15	8.8E-05	3.1E-05	6.0E-05	1.1E+05	7.0E+04	9.1E+04	2.840	48.28%
Saleh 2009****	0.15	8.5E-05	3.0E-05	5.7E-05	1.1E+05	6.8E+04	8.9E+04	2.722	48.20%

*: Accomodation/evaporation coefficient changed from unity to available literature value
**: Background saturation ratio set to 20%
***: Inlet temperature changed to 293K in flow field calculation
****: Partial solution used to obtain the flow field (only temperature)

Recalling Figures 16 and 39 for pimelic acid, it is apparent that the model fitting is not robust since so few points were available to fit (see also Appendix D), so the occurrence of multiple minima is anticipated. Also unsurprisingly, retrieved volatility parameters do not agree well with literature values, and the sensitivity to adjusting the accommodation/evaporation coefficient does not appear realistic. The uncertainty range is low simply because the sensitivity of the parameter estimates is lowered by only considering a few points at low outlet diameters. Observations at lower temperature settings or higher inlet diameters where less volatilization occurs would be needed to better constrain the optimization.

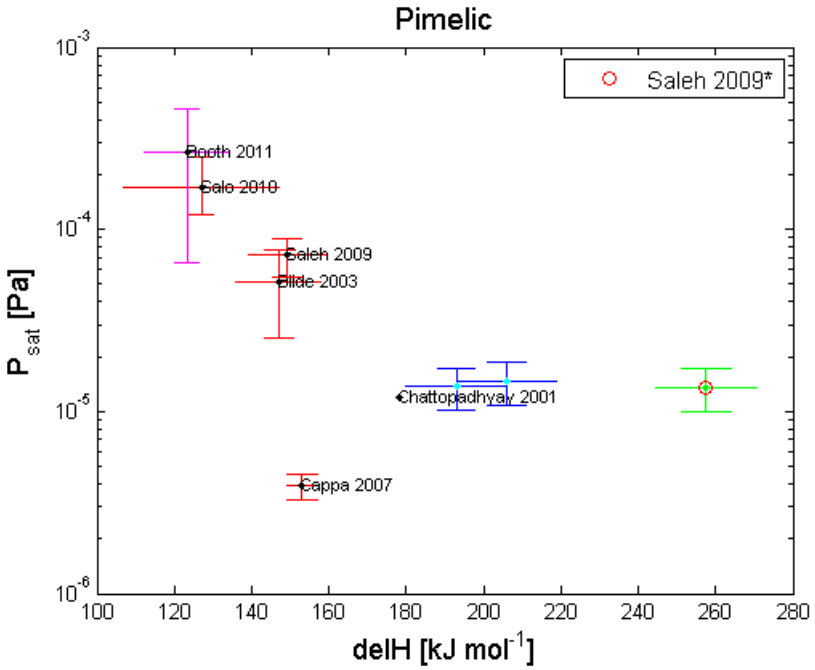

Figure 45: Literature comparison of volatility parameters for pimelic acid

To a similar extent, the results for suberic acid are inconclusive due to the limited volatilization that was observed. As a result, the sensitivity was determined to be much higher than reality. Observations would be needed at higher temperatures to better constrain the uncertainty in the volatility parameters.

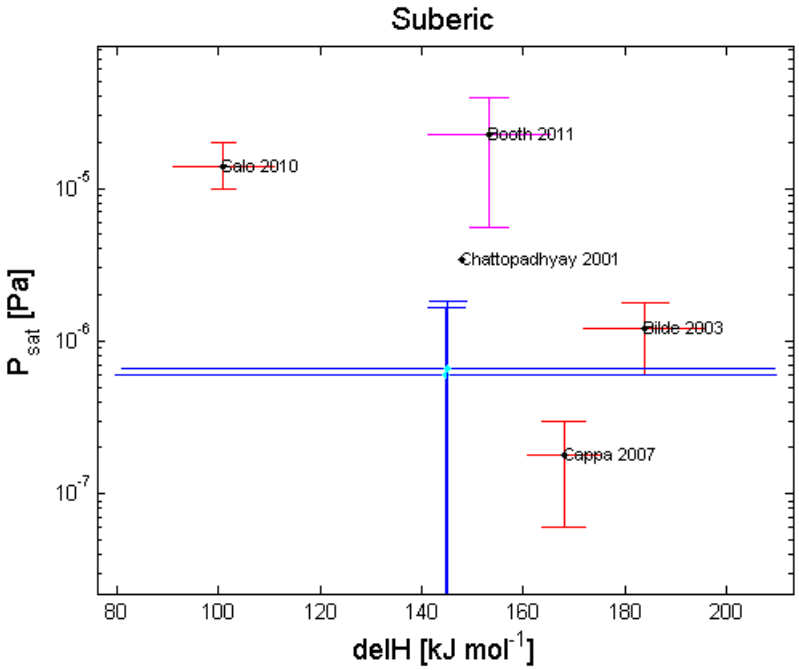

Figure 46: Literature comparison of volatility parameters for suberic acid

Succinic acid, being one of the better characterized compounds in the literature and having ample quality data in this study, was chosen for several sensitivity tests. Estimation of volatility parameters did not appear sensitive to variation of inlet temperature in the flow (black circle), whether or not the partial or full flow field solution was used (red triangle), or if the background saturation ratio was set to 20%. However, adjusting the accommodation/evaporation coefficient resulted in a significant change,

placing it outside the uncertainty range of the other results. The increase uncertainty here is due to the fact that the solution did not actually converge in this case within the cutoff number of iterations. Despite this, the result is consistent with the expected literature value within uncertainty. If the iteration cutoff were increased, the uncertainty would be smaller, but then the result may not necessarily be in agreement with the literature value.

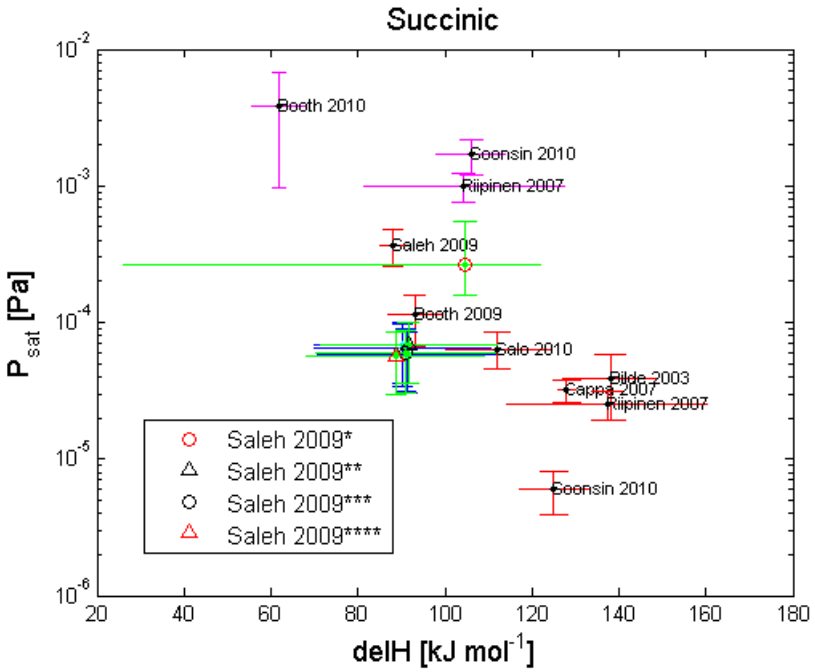

Figure 47: Literature comparison of volatility parameters for succinic acid

Perhaps the major simplifying assumption made in the TD model is that the air surrounding the particle is depleted in the organic vapor (i.e., the partial pressure approaches zero far from the aerosol, $P_{B,\infty} \cong 0$). This implies a kinetic, rather than equilibrium, limitation to the aerosol volatilization in the TD. Given the aerosol generation method and low aerosol mass concentrations in this study, the assumption does not initially appear unrealistic, but quantifying the accuracy of this assumption is

necessary to put the results in perspective. In lieu of coupling the flow field and evaporation modules and performing a more through simulation, calculating the equilibration ratio for the experimental conditions provides an estimate of the error associated with this assumption. The equilibration ratio is essentially a measure of how close conditions approach equilibrium in the TD, where the organic vapor saturates the aerosol's surroundings. At any given point in time, the organic vapor pressure far from the aerosol can be defined as the amount of vapor that initially enters the TD plus the amount that volatilizes from the aerosol phase throughout the TD

$$P_{B,\infty} = P_{B,\infty}(z = 0) + \frac{m_{evap} R T_{\infty}}{M} \tag{18}$$

where m_{evap} is the mass concentration that volatilizes, R is the ideal gas constant, and T_{∞} is the temperature far from the aerosol. Since aerosols in this study are generated by atomization of a solution and drying out the solute, the first term can be assumed to be zero. The assumption that $P_{B,\infty} \cong 0$ can be rephrased as

$$R_n = \frac{P_{B,\infty}}{P^o_{\infty}(T_{\infty})} = \frac{m_{evap} R T_{\infty}}{M P^o_{\infty}(T_{\infty})} \ll 1 \tag{19}$$

where R_n is the equilibration, or saturation, ratio (i.e. relative humidity if considering water vapor). This definition is useful as it provides a quantitative way for the conditions of the experiments to be compared to the underlying assumption: m_{evap} can be calculated from the observed size change of the aerosol and the measured average CPC number concentration, and the saturation vapor pressure can then be varied for the TD temperature setpoints through the use of equation (2). R_n was calculated at the optimized volatility parameters at the points used in the model fitting for each compound investigated, and results are presented in Figures 48-52. Pimelic acid was excluded since its previous results were circumspect. Another important note is that uncertainty ranges

propagated from measurements and are omitted from these figures as they are on the order of 70-80% or more for each point, which would essentially make all calculated uncertainty ranges include $R_n = 1$.

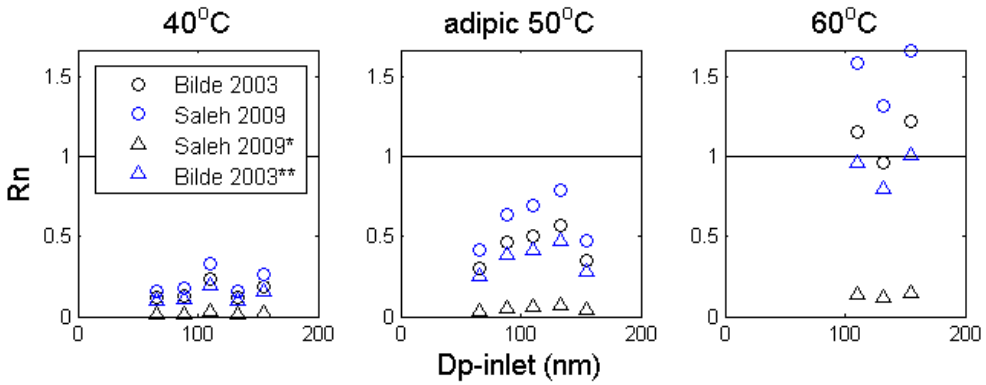

Figure 48: R_n calculation for adipic acid experiments

Adipic and azelaic acid both show significant deviation from the underlying assumption at higher temperature setpoints, exceeding a value of 1, which indicates supersaturation. Realistically the aerosol would, assuming the volatility parameters used here are correct, reach equilibrium within the TD and stop evaporating. However, this is not observed in the data. The sensitivity tests for adipic acid also present interesting results, illustrating that larger vapor pressures obtained from decreased volatilization rates (either through the presence of a nonzero saturation ratio or evaporation coefficient less than unity) tend to have lower values of R_n. Malonic acid appears to agree with the underlying assumption, having low values of R_n for the fitted observations. Suberic acid though appears to disagree greatly with high R_n, almost consistently greater than 1. Of course, the difference between these two is that malonic has a higher vapor pressure and suberic

has a lower vapor pressure, thus the latter requires less volatilization to occur in order to reach high R_n.

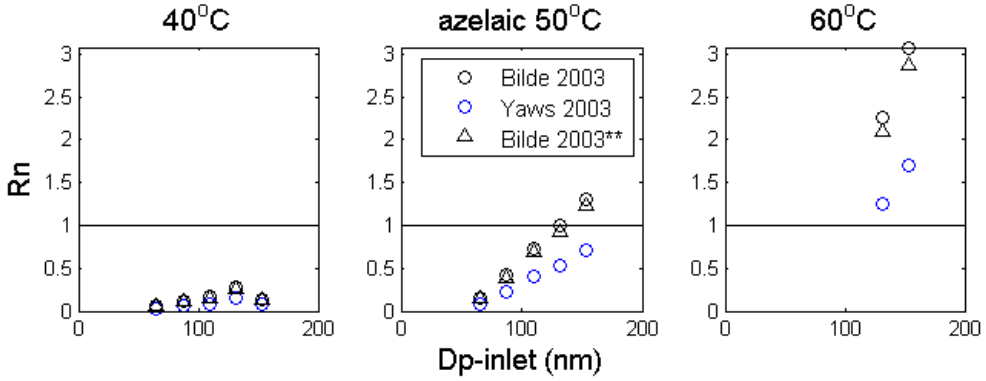

Figure 49: R_n calculation for azelaic acid experiments

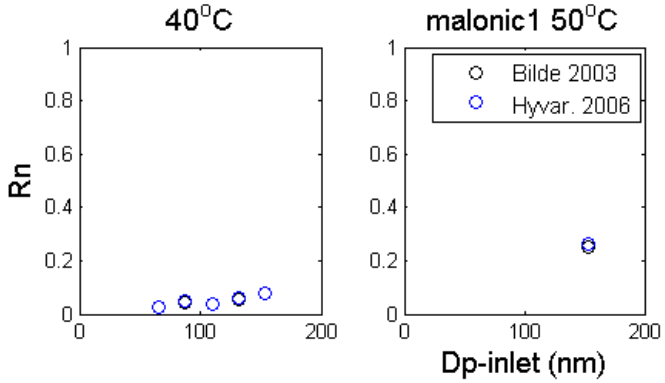

Figure 50: R_n calculation for malonic acid experiments

The results for succinic generally agree with the assumption of low R_n, and the calculation at less than unity evaporation coefficient performs even better. Again, the decrease in R_n is largely due to an increase in the saturation vapor pressure, which is – to some extent – dependent upon the assumption about the background vapor saturation.

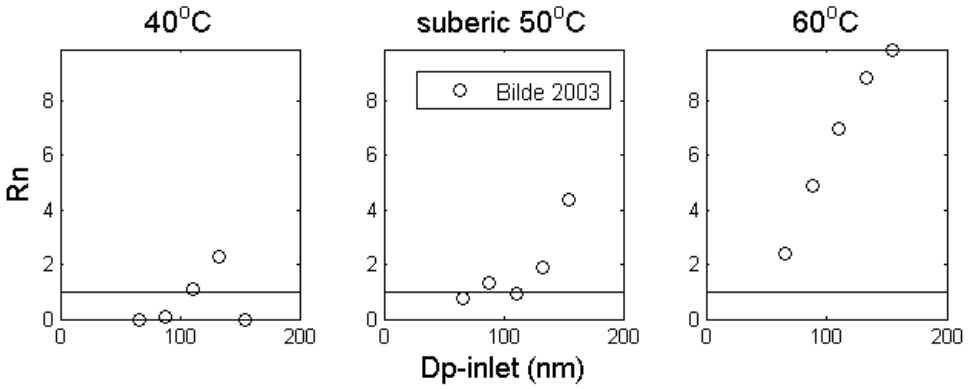

Figure 51: R_n calculation for suberic acid experiments

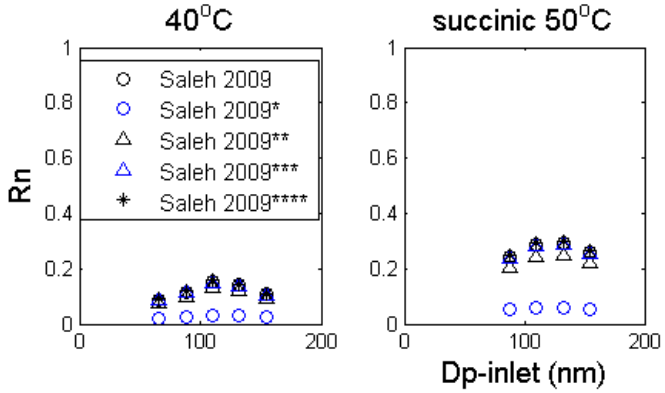

Figure 52: R_n calculation for succinic acid experiments

As appreciable deviation from the assumption of low R_n was observed in the initial experiment results, the sensitivity calculations in Figures 42, 43, and 47 for adipic, azelaic, and succinic acids were performed to see how the volatility parameter estimation responded to a background saturation ratio of 20%. The effect, however, was apparently negligible, especially when compared with the effect of modifying the accommodation/evaporation coefficient. This is not wholly surprising as the level of saturation exceeds 20% in many cases and would vary along the course of the aerosol

volatilization. This sensitivity analysis illustrates that nonzero saturation ratios elevate the estimate of the organic acid's saturation vapor pressure. The choice of an accommodation/evaporation coefficient of unity also implies a lower limit on the aerosol volatility, and fixing a value less than unity raises the saturation vapor pressure estimate. Without knowing a priori the actual equilibration ratio at any given stage of the aerosol volatilization, the setting of an arbitrary value effectively determines the value that would be calculated after the saturation vapor pressure estimation – a sort of circular reasoning. Thus, the need for coupling the TD model components is reinforced by a need to solve the combined problem of a volatilizing aerosol population as it approaches equilibrium.

CHAPTER 4: CONCLUSIONS & FUTURE WORK

In general, the volatility parameters retrieved in this study appear to agree with the literature spread when considering saturation vapor pressure and enthalpy change separately, and a few (e.g. adipic and succinic acid) agree within uncertainty when considering both. The inclusion of the unfitted data that likely represents a non-volatile core in the Figures 35-41 just within the uncertainty bounds of the retrieved volatility parameters reaffirms the parameter fit. If those data were below the limits of the uncertainty range, then the assumption of them being non-volatile cores would be in conflict with the model results. A key note to make however regards the figures for succinc at 60^{o}C and malonic at 50^{o}C where unfitted, supposed non-volatile core data are overlaid with the model prediction. Inlet diameters for which the model predicts a lower or equal value of the outlet diameter is consistent with the assumption of those open circles being non-volatile cores, but an apparent inconsistency is present where the model predicts a larger outlet diameter than what was observed. Since the outlet diameter should be less to be consistent with the observed measurements, this indicates that the model aerosol should be more volatile, either requiring an increase in the reference saturation vapor pressure or the enthalpy of vaporization. This interpretation is consistent with the placement of this study's results for most compounds in the context of literature value comparison presented in Figures 42-47. Pimelic acid is a notable exception, having results that are far more volatile that referenced literature. However, this is likely due to the lack of robust data to fit and is evident in the failure of the optimization routine to find a unique minimum of the cost function

Indirect conclusions regarding the aerosol phase can be made through comparison of the fitted model volatility parameters to the available literature data for solid and liquid phases of the components. The determination of the enthalpy change as referencing vaporization or sublimation could be concluded based on the literature comparison since either combination (saturation vapor pressure over a solid and enthalpy of sublimation or saturation vapor pressure over a liquid and enthalpy of vaporization) can be represented by the same form of equation (2). Also, the use of the Kelvin effect as formulated in equation (1) would be valid for either a liquid or amorphous solid aerosol [Tao and McMurray, 1989]. However, the model does not currently account for variation in surface energy with temperature, and the Kelvin term would need to be modified in order to properly model crystalline aerosol sublimation. However, accurate accounting for the approach to equilibrium within the TD and quantification of the accommodation/evaporation coefficient precludes these types of conclusions, and furthermore, confirmation of aerosol phase and morphology can be made with other independent measurements so as to provide additional degrees of freedom in the volatility analysis.

Modification of the data collection technique would be ideal in order to guarantee quality data and adequate observation of aerosol volatilization. A reactive measurement technique that can check the extent of the size change in real time and adjust selected sizes and temperature setpoints accordingly would be ideal. However, simply including a wider range of sizes and temperatures would also be sufficient, making sure to step to larger inlet diameters at higher temperatures to dodge residual diameter effects. Also, avoiding the re-equilibration of the charge distribution at the second DMA would allow

for a simpler analysis of the measured SMPS distributions. While it may provide additional information on the evaporation when considering mode diameters, re-equilibration of the charge distribution convolutes the data analysis and reduces counting statistics to a detrimental extent. Obtaining inlet and outlet size distributions with physically consistent single modes would also allow for an alternative model fitting procedure utilizing the entire size distribution information (i.e. geometric mean diameter and standard deviation), potentially reducing the uncertainty in optimized parameters.

Though the retrieval of single component volatility parameters did not perfectly align with available literature data, the quantification of the deviation from simplifying assumptions puts these results in perspective and encourages further model development. A more robust fitting of parameters including interfacial energy and the accommodation/evaporation coefficient would be ideal in determining the aerosol volatility. The coupling of a fully resolved flow with a comprehensive aerosol volatilization scheme that can be expanded to treat multicomponent mixtures is the ultimate goal of this work, and it is an ongoing task. The coupling of the TD modules will involve an iterative procedure similar to the one used in Raatikainen et al. [2012] to address water vapor mass balance in the CCN instrument model, where the flow field would first be resolved using the full calculation and then updated with the volatilized organic vapor and temperature fluctuations. From there, additional layers of complexity are to follow: investigating the effect of the cooling section, inclusion of the entire size distribution to improve fitting statistics, optimization of the volatility distribution in the VBS, and addition of mixture non-idealities.

APPENDIX A

EQUATIONS SOLVED FOR FLOW FIELD CALCULATION

The description of the CFD code that determines the flow field properties is presented below in a similar manner as in Nenes et al. [2001].

$$\frac{\partial}{\partial t}(r\rho\phi) + \frac{\partial}{\partial z}(r\rho u\phi) + \frac{\partial}{\partial r}(r\rho v\phi) - \frac{\partial}{\partial z}\left(r\Gamma_\phi \frac{\partial \phi}{\partial z}\right) - \frac{\partial}{\partial r}\left(r\Gamma_\phi \frac{\partial \phi}{\partial r}\right) = S_\phi \quad (20)$$

where the terms are substituted according to Table 3 for the various conserved quantities. Note that in the current form of the flow field module, the heat and organic vapor source terms are not included as the aerosol evaporation module is not coupled to the flow field module.

Table 3: Definition of source terms and transport coefficients for equation (20)

Conserved Quantity	$\boldsymbol{\phi}$	$\boldsymbol{\Gamma_\phi}$	$\boldsymbol{S_\phi}$
Continuity	1	0	0
z – momentum	u	μ	$-r\frac{\partial P}{\partial r} + r\frac{\partial}{\partial z}\left(\mu\frac{\partial u}{\partial r}\right) + \frac{\partial}{\partial r}\left(r\mu\frac{\partial v}{\partial r}\right) + J_{buoy}$
r – momentum	v	μ	$-r\frac{\partial P}{\partial r} + r\frac{\partial}{\partial z}\left(\mu\frac{\partial u}{\partial r}\right) + \frac{\partial}{\partial r}\left(r\mu\frac{\partial v}{\partial r}\right) - \frac{\mu v}{r}$
Heat	T	$\frac{k_a}{c_p}$	$\frac{\Delta \mathrm{H}}{c_p} J_{volat}$
Organic Vapor	m_{evap}	ρD	$-\rho J_{volat}$

The source term for thermal buoyancy effects is defined as:

$$J_{buoy} = -\rho g_{\lambda_2} \left[\frac{T - T_{bulk}(r)}{T_{bulk}(r)}\right] \quad (21)$$

Where g_{λ_2} is the component of gravity in the *r* direction and $T_{bulk}(r)$ is the average temperature along *z* at position *r*.

The source (or sink) term for organic vapor is defined as:

$$J_{volat} = \frac{\pi\rho}{2M} \sum_{i=1}^{n} N_i D_{pi}^2 \frac{dD_{pi}}{dt} \quad (22)$$

Where *n* is the number of size bins in the aerosol distribution with particular diameter and number concentration, and the rate of change is obtained from equation (1) – the aerosol evaporation equation.

APPENDIX B

CALCULATION OF DIFFUSION VOLUMES

The diffusion volumes listed in Table 1 for the organic acids investigated in this work were calculated following the method described in Fuller et. al. [1966].

As an example, consider adipic acid: $C_6H_{10}O_4$

The atomic diffusion volumes from their Table 1 are:
C: 16.5
H: 1.98
O: 5.48

So, the calculation for adipic acid would be: 6*16.5 + 10*1.98 + 4*5.48 =140.72

APPENDIX C

TABLE OF LITERATURE VALUES

Table 4: Literature volatility parameters and associated phase

Source	P_{sat}(298K), Pa			ΔH, J			Sub-Cooled Liquid or Solid?	C*(298K) µg m^{-3}
	Avg.	Max.	Min.	Avg.	Max.	Min.		
Adipic								
Bilde 2003	9.80E-06	1.47E-05	4.90E-06	1.54E+05	1.60E+05	1.48E+05	S	0.578
Saleh 2010[a]	3.30E-05	4.20E-05	2.40E-05	1.32E+05	1.40E+05	1.24E+05	S	1.947
Saleh 2010[h]	4.20E-05	6.40E-05	2.00E-05	1.26E+05	1.47E+05	1.05E+05	S	2.477
Salo 2010	5.80E-05	7.60E-05	4.40E-05	9.70E+04	1.05E+05	8.90E+04	S	3.421
Cappa 2007	2.60E-06	3.60E-06	1.60E-06	1.45E+05	1.50E+05	1.40E+05	S	0.153
Riipinen 2007	4.00E-06	5.00E-06	3.00E-06	1.48E+05*	1.70E+05*	1.26E+05*	S	0.236
Riipinen 2007	1.70E-04	2.00E-04	1.40E-04	1.13E+05	1.35E+05	9.14E+04	L	10.03
Chattopadhyay 2001	1.70E-05	-	-	1.40E+05	-	-	?	1.003
Saleh 2009	3.40E-05	4.60E-05	2.00E-05	1.35E+05	1.48E+05	1.22E+05	S	2.005
Booth 2009	3.28E-06	7.13E-06	-5.70E-07	1.19E+05	1.45E+05	9.30E+04	S	0.193
Booth 2010	2.14E-04	3.75E-04	5.35E-05	8.31E+04	1.09E+05	5.71E+04	L	12.62
Azelaic								
Bilde 2003	6.00E-06	9.00E-06	3.00E-06	1.53E+05	1.77E+05	1.29E+05	S	0.456
Saleh 2010[a]	1.40E-05	1.90E-05	9.00E-06	1.45E+05	1.60E+05	1.30E+05	S	1.064
Saleh 2010[h]	9.00E-06	1.20E-05	6.00E-06	1.58E+05	1.75E+05	1.41E+05	S	0.684
Salo 2010	4.70E-05	5.50E-05	4.00E-05	9.60E+04	1.01E+05	9.10E+04	S	3.571
Cappa 2007	1.00E-08	1.60E-08	4.00E-09	1.78E+05	1.83E+05	1.73E+05	S	0.001

Table 4 (continued)

Malonic								
Bilde 2003	3.60E-04	5.40E-04	1.80E-04	9.20E+04	1.07E+05	7.70E+04	S	15.12
Soonsin 2010	4.30E-04	5.80E-04	2.80E-04	9.60E+04	1.07E+05	8.50E+04	L	18.06
Soonsin 2010	8.00E-05	1.09E-04	5.10E-05	1.07E+05	1.11E+05	1.03E+05	S	3.360
Riipinen 2007	5.20E-05	6.30E-05	4.10E-05	1.41E+05*	1.66E+05*	1.16E+05*	S	2.184
Riipinen 2007	4.90E-04	5.90E-04	3.90E-04	1.22E+05	1.47E+05	9.73E+04	L	20.58
Booth 2009	5.73E-04	6.87E-04	4.59E-04	9.20E+04	9.60E+04	8.80E+04	S	24.07
Booth 2010	3.19E-03	5.58E-03	7.98E-04	7.33E+04	7.73E+04	6.93E+04	L	134.0
Pope 2010	6.70E-04	9.30E-04	5.50E-04	1.42E+05	1.62E+05	1.22E+05	L	28.14
Succinic								
Bilde 2003	3.90E-05	5.85E-05	1.95E-05	1.38E+05	1.49E+05	1.27E+05	S	1.859
Salo 2010	6.40E-05	8.40E-05	4.60E-05	1.12E+05	1.24E+05	1.00E+05	S	3.050
Cappa 2007	3.20E-05	3.80E-05	2.60E-05	1.28E+05	1.30E+05	1.26E+05	S	1.525
Riipinen 2007	2.50E-05	3.10E-05	1.90E-05	1.37E+05*	1.60E+05*	1.14E+05*	S	1.192
Riipinen 2007	9.90E-04	1.23E-03	7.50E-04	1.04E+05	1.27E+05	8.12E+04	L	47.19
Soonsin 2010	1.70E-03	2.20E-03	1.20E-03	1.06E+05	1.14E+05	9.80E+04	L	81.03
Soonsin 2010	6.00E-06	8.10E-06	3.90E-06	1.25E+05	1.33E+05	1.17E+05	S	0.286
Saleh 2009	3.70E-04	4.80E-04	2.60E-04	8.80E+04	9.10E+04	8.50E+04	S	17.64
Booth 2009	1.13E-04	1.60E-04	6.60E-05	9.30E+04	9.90E+04	8.70E+04	S	5.386
Booth 2010	3.86E-03	6.76E-03	9.65E-04	6.17E+04	6.77E+04	5.57E+04	L	184.0

Table 4 (continued)

Suberic								
Bilde 2003	1.20E-06	1.80E-06	6.00E-07	1.84E+05	1.96E+05	1.72E+05	S	0.084
Chattopadhyay 2001	3.40E-06	-	-	1.48E+05	-	-	?	0.239
Salo 2010	1.40E-05	2.00E-05	1.00E-05	1.01E+05	1.11E+05	9.10E+04	S	0.984
Cappa 2007	1.80E-07	3.00E-07	6.00E-08	1.68E+05	1.75E+05	1.61E+05	S	0.013
Booth 2011	2.23E-05	3.90E-05	5.58E-06	1.53E+05	1.65E+05	1.41E+05	L	1.568
Pimelic								
Bilde 2003	5.10E-05	7.65E-05	2.55E-05	1.47E+05	1.58E+05	1.36E+05	S	3.297
Chattopadhyay 2001	1.20E-05	-	-	1.78E+05	-	-	?	0.776
Salo 2010	1.70E-04	2.50E-04	1.20E-04	1.27E+05	1.47E+05	1.07E+05	S	10.99
Cappa 2007	3.90E-06	4.50E-06	3.30E-06	1.53E+05	1.57E+05	1.49E+05	S	0.252
Booth 2011	2.63E-04	4.60E-04	6.58E-05	1.23E+05	1.34E+05	1.12E+05	L	17.00
Saleh 2009	7.20E-05	8.90E-05	5.50E-05	1.49E+05	1.59E+05	1.39E+05	S	4.655

*: Calculated using enthalpy of fusion from Yaws 2003.
[a]: Atomization used as the aerosol generation technique.
[h]: Homogeneous nucleation used as the aerosol generation technique.
Riipinen 2007: solid phase values calculated by using equation and reference values for ΔH_{fus} and heat capacity from liquid results
Booth 2011: liquid values obtained from Bilde estimates of solid values, using other reference data for ΔH_{fus} and $T_{melting}$.

APPENDIX D

MODE DIAMETER DATA TABLES FROM EXPERIMENTS

Data tables for each set of experiments are presented in this appendix. A few abbreviations used as comments are as follows: NV – point omitted due to non-volatile core interference (falls along/near the 1:1 line, see Figures 24-30), MM – point adjusted to an alternative mode considering either or both non-volatile core interference and presence of double-charged particles.

Table 5: Adipic acid average mode diameter data

Adipic T. Set. (^{o}C)	Dp-Inlet	(m) Dp-Obs Raw	Dp-Obs To Fit	Comment
40	6.60E-08	6.15E-08	6.15E-08	
	8.83E-08	8.51E-08	8.51E-08	
	1.11E-07	1.06E-07	1.06E-07	
	1.33E-07	1.29E-07	1.29E-07	
	1.55E-07	1.51E-07	1.51E-07	
50	6.59E-08	4.90E-08	4.90E-08	
	8.82E-08	7.28E-08	7.28E-08	
	1.10E-07	9.47E-08	9.47E-08	
	1.33E-07	1.18E-07	1.18E-07	
	1.55E-07	1.41E-07	1.41E-07	
60	6.58E-08	1.75E-08	-	NV
	8.82E-08	2.25E-08	-	NV
	1.10E-07	2.89E-08	5.73E-08	MM
	1.32E-07	5.98E-08	8.21E-08	MM
	1.54E-07	1.07E-07	1.07E-07	
Remarks: none				

Table 6: Azelaic acid average mode diameter data

Azelaic T. Set. (°C)	Dp-Inlet	(m) Dp-Obs Raw	Dp-Obs To Fit	Comment
40	6.53E-08	5.80E-08	5.80E-08	
	8.75E-08	8.20E-08	8.20E-08	
	1.10E-07	1.06E-07	1.06E-07	
	1.32E-07	1.26E-07	1.26E-07	
	1.53E-07	1.51E-07	1.51E-07	
50	6.53E-08	1.91E-08	3.59E-08	MM
	8.75E-08	6.08E-08	6.08E-08	
	1.10E-07	8.82E-08	8.82E-08	
	1.32E-07	1.13E-07	1.13E-07	
	1.53E-07	1.36E-07	1.36E-07	
60	6.54E-08	1.18E-08	-	NV
	8.76E-08	1.63E-08	-	NV
	1.10E-07	2.09E-08	-	NV
	1.32E-07	2.41E-08	5.60E-08	MM
	1.54E-07	2.76E-08	8.71E-08	MM

Table 7: Glutamic acid average mode diameter data

Glutamic T. Set. (°C)	Dp-Inlet	(m) Dp-Obs Raw	Dp-Obs To Fit	% Change
40	6.55E-08	7.02E-08	-	7.26%
	8.77E-08	9.14E-08	-	4.23%
	1.10E-07	1.13E-07	-	3.30%
	1.32E-07	1.36E-07	-	3.05%
	1.54E-07	1.63E-07	-	5.74%
50	6.55E-08	6.85E-08	-	4.60%
	8.77E-08	9.14E-08	-	4.18%
	1.10E-07	1.13E-07	-	3.20%
	1.32E-07	1.36E-07	-	2.94%
	1.54E-07	1.57E-07	-	1.92%
60	6.56E-08	6.85E-08	-	4.52%
	8.79E-08	9.14E-08	-	3.98%
	1.10E-07	1.13E-07	-	3.12%
	1.32E-07	1.36E-07	-	2.85%
Remarks: All size changes were < 10% (within measurement uncertainty). Also, growth within model TD is unrealistic. Not performing optimization.				

Table 8: Malonic acid average mode diameter data (set #1)

Malonic 1 T. Set. (°C)	Dp-Inlet	(m) Dp-Obs Raw	Dp-Obs To Fit	Comment
40	6.55E-08	1.60E-08	3.30E-08	MM
	8.77E-08	5.43E-08	5.43E-08	
	1.10E-07	8.11E-08	8.11E-08	
	1.32E-07	1.04E-07	1.04E-07	
	1.54E-07	1.29E-07	1.29E-07	
50	6.55E-08	2.59E-08	-	NV
	8.77E-08	3.03E-08	-	NV
	1.10E-07	3.46E-08	-	NV
	1.32E-07	3.52E-08	-	NV
	1.54E-07	3.92E-08	5.27E-08	MM
60	6.55E-08	2.59E-08	-	NV
	8.77E-08	3.00E-08	-	NV
	1.10E-07	3.40E-08	-	NV
	1.32E-07	3.42E-08	-	NV
	1.54E-07	3.85E-08	-	NV

Table 9: Malonic acid average mode diameter data (set #2)

Malonic 2 T. Set. (°C)	Dp-Inlet	(m) Dp-Obs Raw	Dp-Obs To Fit	Comment
40	6.55E-08	3.46E-08	3.46E-08	
	8.76E-08	5.87E-08	5.87E-08	
	1.10E-07	8.51E-08	8.51E-08	
	1.32E-07	1.11E-07	1.11E-07	
	1.54E-07	1.36E-07	1.36E-07	
50	6.55E-08	1.83E-08	-	NV
	8.77E-08	2.17E-08	-	NV
	1.10E-07	2.33E-08	-	NV
	1.32E-07	2.84E-08	-	NV
	1.54E-07	2.96E-08	6.31E-08	MM
60	6.56E-08	1.79E-08	-	NV
	8.78E-08	2.12E-08	-	NV
	1.10E-07	2.33E-08	-	NV
	1.32E-07	2.69E-08	-	NV
	1.54E-07	3.00E-08	-	NV

Table 10: Phthalic acid average mode diameter data

Phthalic T. Set. (^{o}C)	Dp-Inlet	(m) Dp-Obs Raw	Dp-Obs To Fit	% Change
40	6.55E-08	6.85E-08	-	4.61%
	8.77E-08	8.82E-08	-	0.49%
	1.10E-07	1.11E-07	-	1.45%
	1.32E-07	1.36E-07	-	2.99%
	1.54E-07	1.57E-07	-	1.97%
50	6.56E-08	6.61E-08	-	0.84%
	8.78E-08	8.82E-08	-	0.38%
	1.10E-07	1.09E-07	-	-0.53%
	1.32E-07	1.31E-07	-	-0.79%
	1.54E-07	1.57E-07	-	1.81%
60	6.56E-08	6.61E-08	-	0.74%
	8.79E-08	8.82E-08	-	0.26%
	1.10E-07	1.09E-07	-	-0.59%
	1.32E-07	1.31E-07	-	-0.86%
	1.54E-07	1.55E-07	-	0.54%
Remarks: All size changes were < 10% (mea). Not performing optimization.				

Table 11: Pimelic acid average mode diameter data

Pimelic T. Set. (^{o}C)	Dp-Inlet	(m) Dp-Obs Raw	Dp-Obs To Fit	Comment
40	6.59E-08	1.77E-08	-	NV
	8.82E-08	3.09E-08	4.67E-08	MM
	1.10E-07	7.46E-08	7.46E-08	
	1.33E-07	9.82E-08	9.82E-08	
	1.55E-07	1.25E-07	1.25E-07	
50	6.58E-08	1.68E-08	-	NV
	8.81E-08	2.17E-08	-	NV
	1.10E-07	2.69E-08	-	NV
	1.32E-07	3.14E-08	-	NV
	1.54E-07	3.63E-08	-	NV
60	6.59E-08	1.68E-08	-	NV
	8.82E-08	2.17E-08	-	NV
	1.10E-07	2.69E-08	-	NV
	1.32E-07	3.18E-08	-	NV
	1.55E-07	3.59E-08	-	NV
Remarks: Lack of higher T data. Do not expect to obtain a robust parameter fit.				

Table 12: Suberic acid average mode diameter data

Suberic T. Set. (^{o}C)	Dp-Inlet	(m) Dp-Obs Raw	Dp-Obs To Fit	Comment
40	6.59E-08	6.61E-08	6.59E-08	Growth unrealistic.
	8.84E-08	8.82E-08	8.82E-08	
	1.11E-07	1.09E-07	1.09E-07	
	1.33E-07	1.31E-07	1.31E-07	
	1.55E-07	1.57E-07	1.55E-07	Growth unrealistic.
50	6.61E-08	6.15E-08	6.15E-08	
	8.85E-08	8.51E-08	8.51E-08	
	1.11E-07	1.09E-07	1.09E-07	
	1.33E-07	1.31E-07	1.31E-07	
	1.55E-07	1.51E-07	1.51E-07	
60	6.61E-08	1.87E-08	4.09E-08	MM
	8.85E-08	6.86E-08	6.86E-08	
	1.11E-07	9.59E-08	9.59E-08	
	1.33E-07	1.20E-07	1.20E-07	
	1.55E-07	1.44E-07	1.44E-07	
Remarks: Not much volatilization observed. Parameter retrieval doubtful. Capped some values at Dp-Inlet to perform fit because growth in model TD is impossible.				

Table 13: Succinic acid average mode diameter data

Succinic T. Set. (^{o}C)	Dp-Inlet	(m) Dp-Obs Raw	Dp-Obs To Fit	Comment
40	6.57E-08	5.23E-08	5.23E-08	
	8.80E-08	7.64E-08	7.64E-08	
	1.10E-07	9.82E-08	9.82E-08	
	1.32E-07	1.22E-07	1.22E-07	
	1.54E-07	1.46E-07	1.46E-07	
50	6.57E-08	2.25E-08	-	NV
	8.80E-08	2.94E-08	5.27E-08	MM
	1.10E-07	7.91E-08	7.91E-08	
	1.32E-07	1.02E-07	1.02E-07	
	1.54E-07	1.26E-07	1.26E-07	
60	6.45E-08	1.51E-08	-	NV
	8.67E-08	1.99E-08	-	NV
	1.09E-07	2.41E-08	-	NV
	1.31E-07	2.89E-08	-	NV
	1.54E-07	3.46E-08	-	NV

REFERENCES

An, W. J., Pathak, R. K., Lee, B. H. Pandis, S. N. (2007). Aerosol volatility measurement using an improved thermodenuder: Application to secondary organic aerosol. *J. Aeros. Sci.*, 48, 305-314.

Bilde, M., Pandis, S. N. (2001). Evaporation Rates and Vapor Pressures of Individual Aerosol Species Formed in the Atmospheric Oxidation of α- and β-Pinene. *Environ. Sci. Technol.*, 35, 3344.

Bilde, M., Svenningsson, B., Mønster, J., Rosenørn, T. (2003). Even-Odd Alternation of Evaporation Rates and Vapor Pressures of C3-C9 Dicarboxylic Acid Aerosols. *Envrion. Sci. Technol.*, 37, 1371.

Bird, R. B., Stewart, W. E., and Lightfoot, E. N. (2002). *Transport Phenomena* (2nd ed.), New York, NY: John Wiley & Sons, Inc.

Booth, A. M., Markus, T., McFiggans, G., Percival, C. J., McGillen, M. R., and Topping, D. O. (2009). Design and construction of a simple Knudsen Effusion Mass Spectrometer (KEMS) system for vapour pressure measurements of low volatility organics, *Atmos. Meas. Tech.*, 2, 355-361.

Booth, A. M., Barley, M. H., Topping, D. O., McFiggans, G., Garforth, A., and Percival, C. J. (2010). Solid state and sub-cooled liquid vapor pressures of substituted dicarboxylic acids using Knudsen Effusion Mass Spectrometry (KEMS) and Differential Scanning Calorimetry, *Atmos. Chem. Phys.*, 10, 4879-4892.

Booth, A. M., Montague, W. J., Barley, M. H., Topping, D. O., McFiggans, G., Garforth, A., Percival, C. J. (2011). Solid state and sub-cooled liquid vapor pressures of cyclic aliphatic dicarboxylic acids, *Atmos. Chem. Phys.*, 11, 655-665.

Brown, P.N., Byrne, G.D., Hindmarsh, A.C. (1989). VODE, a variable-coefficient ODE solver, *SIAM Journal on Scientific and Statistical Computing*, 10, 1038–1051.

Cappa, C. D. (2010). A model of aerosol evaporation kinetics in a thermodenuder. *Atmos. Meas. Tech.*, 3, 579-592, doi:10.5194/amt-3-579-2010.

Cappa, C. D. and Jimenez, J. L. (2010). Quantitative estimates of the volatility of ambient organic aerosol, *Atmos. Chem. Phys.*, 10, 5409-5424, doi:10.5194/acp-10-5409-2010.

Cappa, C. D., Lovejoy, E. R. and Ravishankara, A. R. (2007). Determination of Evaporation Rates and Vapor Pressures of Very Low Volatility Compounds: A Study of the C_4-C_{10} Dicarboxylic Acids. *J. Phys. Chem.*, 111, 3099-3109.

Cerully, K. M., Hite, J. R., McLaughlin, M., Nenes, A. Combined Aerosol Hygroscopicity and Volatility Measurements: Pt. 1 – Analysis of a New Measurement Method to Infer Organic Aerosol Volatility. In Prep.

Chattopadhyay, S., Tobias, H. J., Ziemann, P. J. (2001). A Method for Measuring Vapor Pressures of Low-Volatility Organic Aerosol Compounds Using a Thermal Desorption Particle Beam Mass Spectrometer, *Anal. Chem.*, 73, 3797-3803.

Chen, N. H., Othmer, D. F. (1962). New Generalized Equation for Gas Diffusion Coefficient. *J. Chem. Eng. Data*, 7, 37-41.

Donahue, N. M., Robinson, A. L., and Pandis, S. N. (2009). Atmospheric organic particulate matter: From smoke to secondary organic aerosol. *Atmos. Env.*, 43, 94-106.

Donahue et al., N. M., Robinson, A. L., Stanier, C. O., and Pandis, S. N. (2006). Coupled partitioning, dilution, and chemical aging of semivolatile organics. *Env. Sci. Tech.*, 40, 2635-2643, doi:10.2012/es052297c.

Faulhaber, A. E., Thomas, B. M., Jiminex, J. L., Jayne, J. T., Worsnop, D. R., and Ziemman, P. J. (2009). Characterization of a thermodenuder-particle beam mass spectrometer system for the study of organic aerosol volatility and composition, *Atmos. Chem. Phys.*, 2, 15-31.

Fierz, M., Vernooij, M. G. C., and Burtscher, H. (2007). An improved low-flow thermodenuder. *Aeros. Sci.*, 38, 1163-1168.

Fuchs, N. A., and Sutugin, A. G. (1971) High dispersed aerosols, in *Topics in Current Aerosol Research (Part 2)*, G. M. Hidy and J. R. Brock, eds., Pergamon, New York, pp. 1-200.

Fuentes, E., and McFiggans, G. (2012). A modeling approach to evaluate the uncertainty in estimating evaporation behavior and volatility of organic aerosols. *Atmos. Meas. Tech.*, 5, 735-757, doi:10.5194/amt-5-735-2012.

Fuller, E.N., Schettle, Pd, Giddings, J.C., (1966). A new method for prediction of binary gas-phase diffusion coeffecients. *Ind. Eng. Chem.* 58. 19.

Hallquist, M., Wenger, J. C., Baltensperger, U., Rudich, Y., Simpson, D., Claeys, M., Dommen, J., Donahue, N. M., George, C., Goldstein, A. H., Hamilton, J. F., Herrmann, H., Hoffmann, T., Iinuma, Y., Jang, M., Jenkin, M. E., Jimenez, J. L., Kiendler-Scharr, A., Maenhaut, W., McFiggans, G., Mentel, Th. F., Monod, A., Prévôt, A. S. H., Seinfeld, J. H., Surratt, J. D., Szmigielski, R., and Wildt, J. (2009). The formation, properties and impact of secondary organic aerosol: current and emerging issues. *Atmos. Chem. Phys.*, 9, 5155-5236.

Hite, J. R., Cerully, K. M., Nenes, A. Combined Aerosol Hygroscopicity and Volatility Measurements: Pt. 2 – Retrieval of Volatility Distributions for Multicomponent Aerosol. In Prep.

Huffman, J. A., Ziemann, P. J., Jayne, J. T., Worsnop, D. R., and Jimenez, J. L. (2008). Development and Characterization of a Fast-Stepping/Scanning Thermodenuder for Chemically-Resolved Aerosol Volatility Measurements. *Aeros. Sci. Tech.*, 42, 395-407.

Hyvärinen, A.-P., Lihavainen, H., Gaman, A., Vairila, L., Ojala, H., Kulmala, M., Viisanen, Y. (2006). Surface Tensions and Densities of Oxalic, Malonic, Succinic, Maleic, Malic, and cis-Pinonic Acids, *J. Chem. Eng. Data*, 51, 255.

International Mathematical and Statistical Library, Houston Texas, (program IMSL-ZXSSQ).

IPCC (2007). *Climate Change 2007: Synthesis Report. Contribution of Working Groups I, II and III to the Fourth Assessment Report of the Intergovernmental Panel on Climate Change* [Core Writing Team, Pachauri, R. K. and Reisinger, A. (eds.)]. IPCC, Geneva, Switzerland.

Jimenez, J.L., Canagaratna, M. R., Donahue, N. M., Prévôt, A. S. H., Zhang, Q., Kroll, J. H., DeCarlo, P. F., Allan, J. D., Coe, H., Ng, N. L., Aiken, A. C., Docherty, K. S., Ulbrich, I. M., Grieshop, A. P., Robinson, A. L., Duplissy, J., Smith, J. D., Wilson, K. R., Lanz, V. A., Hueglin, C., Sun, Y. L., Tian, J., Laaksonen, A., Raatikainen, T., Rautiainen, J., Vaattovaara, P., Ehn, M., Kulmala, M., Tomlinson, J. M., Collins, D. R., Cubison, M. J., Dunlea, E. J., Huffman, J. A., Onasch, T. B., Alfarra, M. R., Williams, P. I., Bower, K., Kondo, Y., Schneider, J., Drewnick, F., Borrmann, S., Weimer, S., Demerjian, K., Salcedo, D., Cottrell, L., Griffin, R., Takami, A., Miyoshi, T., Hatakeyama, S., Shimono, A., Sun, J. Y., Zhang, Y. M., Dzepina, K., Kimmel, J. R., Sueper, D., Jayne, J. T., Herndon, S. C., Trimborn, A. M., Williams, L. R., Wood, E. C., Middlebrook, A. M., Kolb, C. E., Baltensperger, U., and Worsnop, D. R. (2009). Evolution of Organic Aerosols in the Atmosphere. *Science*, 326, 1525-1529.

Kanakidou, M., Seinfeld, J. H., Pandis, S. N., Barnes, I., Dentener, F. J., Facchini, M. C., Van Dingenen, R., Ervens, B., Nenes, A., Nielsen, C. J., Swietlicki, E., Putaud, J. P., Balkanski, Y., Fuzzi, S., Horth, J., Moortgat, G. K., Winterhalter, R., Myhre, C. E. L., Tsigaridis, K., Vignati, E., Stephanou, E. G., and Wilson, J. (2005). Organic Aerosol and Global Climate Modelling: A Review. *Atmos. Chem. Phys.*, 5, 1053–1123.

National Instruments: LabVIEW software. http://www.ni.com/labview

Nenes, A., P. Y. Chuang, R. C. Flagan, and J. H. Seinfeld (2001) A theoretical analysis of cloud condensation nucleus (CCN) instruments, *J. Geophys. Res.*, 106(D4), 3449–3474, doi:10.1029/2000JD900614.

Orsini, D. A., Wiedensohler, A., and Stratmann, F. (1998). A New Volatility Tandem Differential Mobility Analyzer to Measure the Volatile Sulfuric Acid Aerosol Fraction. *J. Atmos. Ocean. Tech.*, 16, 760-772.

Pankow, J. F. (1994). An absorption model of gas/particle partitioning or organic compounds in the atmosphere. *Atmos. Env.*, 28, 185-188.

Patankar, S. V. (1980). Numerical Heat Transfer and Fluid Flow. McGraw-Hill, New York

Pope, F. D., Tong, H., Dennis-Smither, B. J., Griffiths, P. T., Clegg, S. L., Reid, J. P., Cox, R. A. (2010). Studies of Single Aerosol Particles Containing Malonic Acid, Glutaric Acid, and Their Mixtures with Sodium Chloride. II. Liquid-State Vapor Pressures of the Acids, *J. Phys. Chem. A*, 114, 10156-10165.

Raatikainen, T., Moore, R. H., Lathem, T. L., and Nenes, A. (2012) A coupled observation – modeling approach for studying activation kinetics from measurements of CCN activity, *Atmos. Chem. Phys.*, 12, 4227-4243, doi:10.5194/acp-12-4227-2012.

Rader, D. J., and McMurry, P. H. (1986). Application of the tandem differential mobility analyzer to studies of droplet growth or evaporation, *J. Aeros. Sci.*, 17, 771-787. doi:10.1016/0021-8502(86)90031-5.

Ravindran, P., Davis, E. J., Ray, A. K. (1979). Diffusivities of Low-Volatility Species in Light Gases. *AIChE J*., 25, 966-975.

Riipinen, I., Koponen, I. K., Frank, G. P., Hyvarinen, A.-P., Vanhanen, J., Lihavainen, H., Lehtinen, K. E. J., Bilde, M.., Kulmala, M.., (2007) Adipic and malonic acid aqueous solutions: surface tensions and saturation vapor pressures. *J. Phys. Chem*., 111 (50), 12995–13002.

Riipinen, I., Pierce, J. R., Donahue, N. M., and Pandis, S. N. (2010). Equilibration time scales of organic aerosol inside thermodenuders: Evaporation kinetics versus thermodynamics. *Atmos. Env.*, 44, 597-607.

Riipinen, I., Pierce, J. R., Yli-Juuti, T., Nieminen, T., Häkkinen, S., Ehn, M., Junninen, H., Lehtipalo, K., Petäjä, T., Slowik, J., Chang, R., Shantz, N. C., Abbatt, J., Leaitch, W. R., Kerminen, V.-M., Worsnop, D. R., Pandis, S. N., Donahue, N. M., and Kulmala, M. (2011). Organic condensation: a vital link connecting aerosol formation to cloud condensation nuclei (CCN) concentrations, *Atmos. Chem. Phys.*, 11, 3865-3878, doi:10.5194/acp-11-3865-2011.

Saleh, R. and Shijadeh, A. (2007). Hygroscopic growth and evaporatioin in an aerosol with boundary heat and mass transfer. *Aeros. Sci.*, 38, 1-16.

Saleh, R., Shihadeh, A., and Khlystov, A. (2010). Effect of Aerosol Generation Method on Measured Saturation Pressure and Enthalpy of Vaporization of Dicarboxylic Acid Aerosols. *Aerosol Sci. Technol*., 44, 302–307.

Saleh R., Walker J., Khlystov A. (2008), Determination of saturation pressure and enthalpy of vaporization of semi-volatile aerosols: The integrated volume method, *J. Aeros. Sci.*, 39, 10, 876-887.

Saleh R., Shihadeh A., Khlystov A. (2009), Determination of evaporation coefficients of semi-volatile organic aerosols using an integrated volume—tandem differential mobility analysis (IV-TDMA) method, *J. Aeros. Sci.*, 40, 12, 1019-1029.

Saleh, R., Shihadeh, A., and Khlystov, A. (2011). On transport phenomena and equilibration time scales in thermodenuder. *Atmos. Meas. Tech.*, 4, 571-581, doi:10.5194/amt-4-571-2011.

Salo, K.; Jonsson, A. M.; Andersson, P. U.; Hallquist, M. (2010), Aerosol Volatility and Enthalpy of Sublimation of Carboxylic Acids. *J. Phys. Chem. A*, 114, 4586−4594.

Salo, K., Hallquist, M., Jonsson, Å. M., Saathoff, H., Naumann, K.-H., Spindler, C., Tillmann, R., Fuchs, H., Bohn, B., Rubach, F., Mentel, Th. F., Müller, L., Reinnig, M., Hoffmann, T., and Donahue, N. M. (2011). Volatility of secondary organic aerosol during OH radical induced ageing. *Atmos. Chem. Phys.*, 11, 11055-11067.

Seinfeld, J. H. and Pandis, S. (2006) Atmospheric Chemistry and Physics: from air pollution to climate change, Hoboken, N.J.: J. Wiley, 2nd ed.

Soonsin, V., Zardini, A. A., Marcolli, C., Zuend, A., and Krieger, U. K. (2010). The vapor pressures and activities of dicarboxylic acids reconsidered: the impact of the physical state of the aerosol, *Atmos. Chem. Phys*., 10, 11753-11767, doi:10.5194/acp-10-11753-2010.

Tao, Y. and McMurry, P. (1989). Vapor Pressures and Surface Free Energies of C14-C18 Monocarboxylic Acids and C5 and C6 Dicarboxylic Acids. *Environ. Sci. Technol.*, 23, 1519.

Tsimpidi, A. P., Karydis, V. A., Zavala, M., Lei, W., Molina, L., Ulbrich, I. M., Jimenez, J. L., and Pandis, S. N. (2010) Evaluation of the volatility basis-set approach for the simulation of organic aerosol formation in the Mexico City metropolitan area, Atmos. Chem. Phys., 10, 525-546

Yaws, Carl L. (2003). Yaws' Handbook of Thermodynamic and Physical Properties of Chemical Compounds. Knovel.